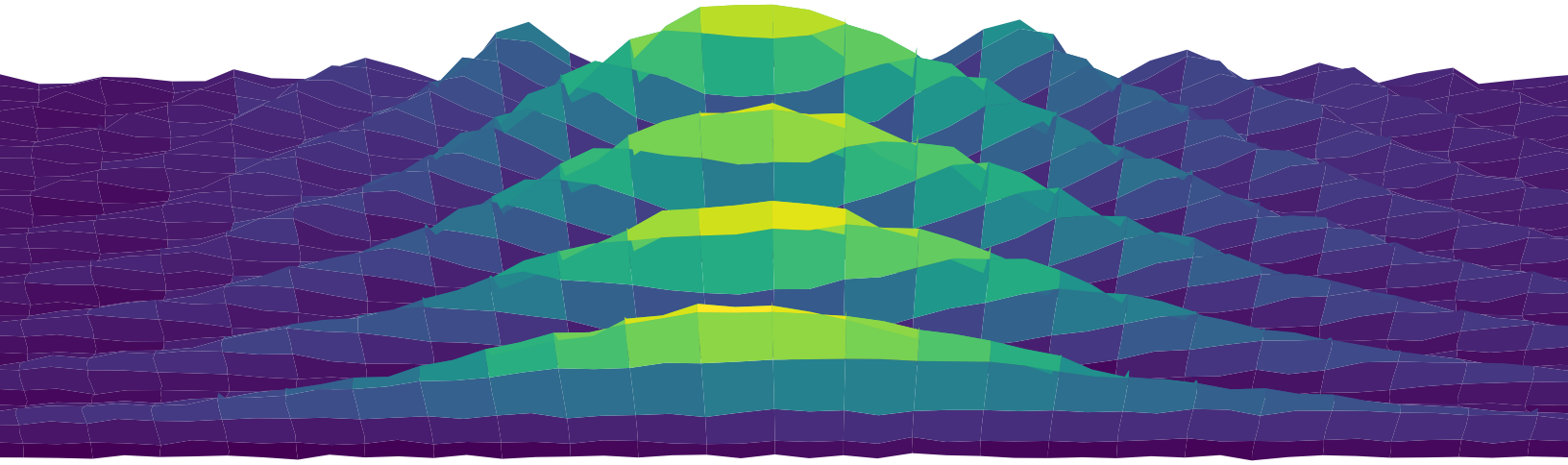

Shaping of Fast Flux Pulses for Two-Qubit Gates

Inverse Filtering

Jonas Butscher

Supervisor: Dr. Sebastian Krinner
Professor: Prof. Andreas Wallraff

Master's Thesis

Quantum Device Lab
ETH Zürich
January 4, 2018

Abstract

It is essential to have a universal set of well scalable, high-fidelity quantum gates to successfully perform quantum algorithms and especially to reach the error threshold for quantum error correction codes. In this thesis, I work towards the automated tune up of a flux pulse based controlled-phase gate in a superconducting circuit architecture [Strauch2003, DiCarlo2009]. To optimize the gate fidelity, we develop a procedure to correct for distortions affecting the flux pulses focusing on the scalability aspect and the use in the surface error correction code. In particular, I elaborate a method to shape flux pulses based on a combination of finite impulse response (FIR) filters and infinite impulse response (IIR) filters which invert distortions on a nanosecond timescale and on a slower timescale up to microseconds, respectively. The latter are used to efficiently reduce memory effects in the flux line that originate from the use of a bias-T and adversely affect subsequent gates [Kelly2014].

Contents

Chapter 1

Introduction

Already decades ago, in the early 80s, Richard Feynman asked the question: "What kind of computer are we going to use to simulate physics?" [Feynman1982]. For the simulation of quantum systems, the computational demands on a classical computer grow exponentially with the system size. As a consequence, the idea of using quantum mechanical systems to encode information and perform calculations arose. Since then, the new field called Quantum Computing emerged. In addition, fundamentally new ideas were developed, how to parallelize classical calculations using the quantumness of the information processing unit, e.g., Shor's factoring algorithm [Shor1994]. The concept of quantum information processing gained even more importance, as it was realized, that classical computers start to touch the limits of physical miniaturization, also referred to as the break down of Moore's law [Moore1965].
However, it is still an open question, if quantum computers can by physically implemented in a way, that they can beat classical computers, i.e., that they prove quantum supremacy [Preskill2012]. A physical realization of a quantum information carrier should be well isolated from its environment, to prevent loss and decoherence, while still couple strongly to some control fields, which allow the qubit to be manipulated in a coherent way and be coupled to other qubits in a scalable way. Some of the most promising implementations currently under development are trapped ions [Cirac1995], nitrogen vacancy centers [Dutt2007] and superconducting electronic circuits [Clarke2008].

1.1 Quantum Computing

In quantum information theory, the natural choice for the basic entity that carries quantum information is a quantum mechanical two-level system, a quantum bit or qubit, in close analogy to the bit in classical computation. A classical bit represents a single binary digit, that can assume the values 0 and 1, whereas a qubit has the basis states $|0\rangle$ and $|1\rangle$ and is represented by a wavefunction $|\psi\rangle = a\,|0\rangle + b\,|1\rangle$, where a and b can be any pair of complex numbers satisfying the normalization condition $|a|^2 + |b|^2 = 1$. An example for such a quantum system with a two dimensional Hilbert space $\mathbb{C}^2$ is a spin 1/2 system, e.g., the spin degree of freedom of a single electron.
Quantum algorithms are usually described as quantum circuits (for an example see Fig. 1.1), a set of quantum gates applied to the qubits in a specific order. A set of gates, that generates all possible quantum gates, is called a set of universal quantum gates. I.e., any quantum algorithm can be executed, if a set of universal quantum gates is physically accessible.

1.1.1 Error correction

A qubit must couple to some control field to be manipulated. In addition to coupling to the vacuum, all interaction with its noisy environment introduces loss and dephasing. Unlike classical computers, a quantum memory can not simply be refreshed by reading it out and overwriting it again, as it is standard for dynamic random-access memory (DRAM) [Laplante1999]. Due to the complementarity of quantum measurements, the readout of a qubit can never extract its full information. To overcome this difficulty, a diversity of so-called quantum error correction (QEC) codes were developed, e.g. the Shor code [Shor1995]. The basic idea of such QEC codes is to build a logical qubit out of multiple physical qubits in a clever way, such that parity measurements on a set of these physical qubits give information about errors, but do not destroy the quantum information. In other words, the error syndrome measurements are chosen such that the logical qubit states are eigenstates of the measurement operators, also called stabilizers, and get projected back into the logical subspace by the error syndrome measurement. Depending on the complexity of the QEC code, it can handle a different error probability. Both the quality of the qubit operations, called gate fidelity, and the time of an error correction cycle are critical and defining for the so-called error correction threshold. This threshold, which states the minimal requirements on the physical implementation of qubits and gates, depends also strongly on the type of the QEC code. One class of error correction codes are the topological quantum codes [Kitaev1996, Bombin2013]. These QEC codes rely only on local interconnectivity, as for example the surface code which is based on a two-dimensional grid of qubits with nearest neighbor interaction [Raussendorf2007, Terhal2013]. Together with its relative high error robustness the surface code is a good candidate to be implemented in a superconducting quantum computer architecture [Fowler2012].

1.1.2 Multi-Qubit Operations

For any kind of quantum computation and error correction code, the ability to do multi-qubit operations is crucial. Only when generating a special kind of quantum states, so-called entangled states, the full capability of quantum computing is unveiled. More formally spoken, every set of universal quantum gates contains at least one two-qubit gate [Nielsen2000].

Two-Qubit gates

The simplest generators of multi-qubit gates are two-qubit gates, as for example the controlled-NOT or the controlled-phase gate (see also Fig. 1.1). Controlled gates work like their classical analogue. A unitary operation on a target qubit is executed only if another qubit, the control qubit, is in a specific state, usually the excited state. If the control qubit is in a superposition state, then the controlled gate will entangle the target qubit with the control qubit.

In our research group, we are specialized on superconducting transmon qubits first described in [Koch2007]. Ref. [Majer2007] proposed how to couple these kind of qubits together via a cavity bus. Since then, different ways to perform two-qubit gates have been shown, e.g. gates based on sideband transitions [Wallraff2007, Leek2009], cross-resonance gates [Chow2011, Sheldon2016] and fast flux gates [DiCarlo2009, DiCarlo2010, Barends2014]. An advantage of all-microwave gates is, that the qubits always stay at their optimal bias point with minimal dephasing. On the downside, these gates are in general more than an order of magnitude slower than flux gates. Regarding QEC, gate fidelity and short gate times are essential to surpass the error correction

threshold. This is why we chose the latter approach.

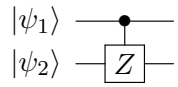

Fig. 1.1: Quantum circuit of a C-Phase gate on the initial two-qubit state $|\psi_1\rangle \otimes |\psi_2\rangle$.

1.2 Motivation

In this respect, the goal of this thesis is to work towards high fidelity, scalable two-qubit gates extending the approach described in [Strauch2003, DiCarlo2009, DiCarlo2010]. As part of the surface code project with the final goal to run the surface-49 code [Versluis2017, Horsman2012], we develop gates, that can be applied repeatedly without the need of individual gate calibration, i.e., that are scalable. For the two-qubit gate we are planning to implement, we need to provide fast current pulses with an arbitrary waveform generator (AWG) with low noise and minimal distortion. To reduce the $1/f$ noise characteristic for AWGs, we use a high-pass filter which introduces distortions on a timescale two orders of magnitude slower than the gate time. For any real time quantum operation, as for example a QEC cycle, the gate sequence is not predetermined. Hence, for the cancellation of the slow distortions caused by the high-pass filter, we rely on real time inverse filtering. For this purpose, we elaborate a predistortion filter scheme together with our partner Zurich Instruments which allows for real time filtering of the flux pulses.

Chapter 2

Circuit Quantum Electrodynamics: Two-qubit flux gates

In this chapter, I briefly elaborate the theoretical background of circuit quantum electrodynamics (cQED) used in the experiments. I will focus on the transmon qubit dispersively coupled to a readout resonator and a cavity bus, summarizing the references [Baur2012b, Steffen2013a, Koch2007, Majer2007].

2.1 cQED basics

In circuit quantum electrodynamics the classical equations of motion can be deduced from the classical Kirchhoff rules. When writing down these equations in terms of flux and charge variables, a Hamiltonian can be found describing the system classically. The quantum mechanical description is obtained by imposing canonical quantization conditions on the flux and charge variables [Yurke1984, Devoret1997, Devoret2004]. This procedure allows to find the Schroedinger equations for any superconducting circuit.

2.1.1 The Transmon Qubit

Superconducting circuits composed of inductances and capacitances are all linear and have harmonic modes as solutions. The essential ingredient to build non-linear, dissipation free, atom-like structures is the Josephson junction [Devoret2004]. Proposed in 2007 by [Koch2007], the transmon qubit proved to be very successful. It consists of a superconducting island connected to a reservoir of Cooper pairs by a capacitively shunted SQUID loop (two parallel Josephson junctions) behaving like an anharmonic oscillator. The SQUID allows for tunability of the Josephson energy $E_J = E_J^{\max}|\cos(\pi\Phi/\Phi_0)|$, where $E_J^{\max}$ is the maximal Josephson energy, Φ is the external flux through the SQUID loop and $\Phi_0 = h/2e$ is the superconducting flux quantum with Planck constant h and Cooper pair charge $2e$. The charging energy $E_C = e^2/2C_\Sigma$ is defined by the total capacitance C_Σ between the superconducting island and reservoir. The transmon's recipe for success is the exponential suppression of charge noise for large E_J/E_C due to its flattened charge dispersion relation while sill having sufficient anharmonicity which only decreases polynomially with growing E_J/E_C. The anharmonicity α is defined as $\alpha = E_{12} - E_{01} \approx -E_C$ where E_{ij} is the transition energy from state $|i\rangle$ to $|j\rangle$. On one hand, the insensitivity to charge noise allows for long coherence times while on the other hand the finite anharmonicity is necessary

to selectively address the two energetically lowest eigenstates $|0\rangle$ and $|1\rangle$, the logical qubit states. Tuning of the Josephson energy by en external magnetic flux allows for dynamic changes of the qubit frequency given by [Koch2007]

$$\hbar\omega_q = E_{01} = \sqrt{8E_J^{\max}E_C|\cos(\pi\Phi/\Phi_0)|} - E_C. \tag{2.1}$$

The maximum frequency is usually called 'sweet spot', since the qubit parked at this frequency is first-order insensitive to flux noise and thus has better coherence times. In this two level approximation, the qubit can be described by the Hamiltonian

$$\widehat{H}_q = \frac{\hbar\omega_q}{2}\hat{\sigma}^z, \qquad \hat{\sigma}^z = \begin{pmatrix}1 & 0\\ 0 & -1\end{pmatrix}, \quad |0\rangle = \begin{pmatrix}0\\1\end{pmatrix}, \quad |1\rangle = \begin{pmatrix}1\\0\end{pmatrix}, \tag{2.2}$$

where $\hat{\sigma}^z$ is the Pauli-Z operator.

Applying a coherent microwave field across the Josephson junctions close to resonance with the qubit, adds a transverse term of the form [Steffen2013a]

$$\hat{H}_{\text{drive}} = \frac{\Delta}{2}\hat{\sigma}^z + \frac{\Omega(t)}{2}\left(\cos(\phi)\hat{\sigma}^x + \sin(\phi)\hat{\sigma}^y\right) \tag{2.3}$$

to the Hamiltonian, where ϕ is the phase of the drive field detuned by $\Delta = \omega_q - \omega_d$ w.r.t the qubit and $\Omega(t) \propto \mathcal{E}(t)$ is the Rabi frequency proportional to the drive amplitude $\mathcal{E}(t)$. $\hat{\sigma}^x$ and $\hat{\sigma}^y$ are the Pauli-X and -Y operators, respectively:

$$\hat{\sigma}^x = \begin{pmatrix}0 & 1\\ 1 & 0\end{pmatrix}, \qquad \hat{\sigma}^y = \begin{pmatrix}0 & -i\\ i & 0\end{pmatrix}. \tag{2.4}$$

This allows to apply arbitrary single qubit rotations around any axis lying in the x-y plane by choosing a resonant drive $\Delta = 0$ with appropriate phase ϕ.

2.1.2 Qubit Readout in the Dispersive Regime

Coupling the island of the transmon qubit capacitively to a coplanar waveguide resonator, lets the qubit interact with the harmonic modes of the resonator in the strong coupling regime. The quantum mechanical system is described to a good approximation by the generalized Jaynes-Cummings Hamiltonian [Koch2007]

$$\hat{H}_{\text{JC}} = \hbar\omega_r\hat{a}^\dagger\hat{a} + \hbar\sum_j \omega_j |j\rangle\langle j| + \hbar\sum_i \left(g_{i,i+1}|i\rangle\langle i+1|\hat{a}^\dagger + \text{h.c.}\right), \tag{2.5}$$

taking also higher transmon states $|j\rangle$ with energy $\hbar\omega_j$ into account. The resonator, described by its annihilation and creation operators $\hat{a}$ and $\hat{a}^\dagger$ with frequency $\omega_r/2\pi$, couples to the transmon levels $|j\rangle$ and $|j+k\rangle$ with coupling strength $g_{j,j+k}$, where $k = \pm 1$. Transitions with $k > 1$ are highly suppressed for large E_J/E_C [Koch2007].

The dispersive limit is the parameter regime, where the detuning $\Delta = \omega_q - \omega_r$ between the qubit and the resonator is much larger than the coupling energy, i.e., $g_{01}/|\Delta| \ll 1$. Expanding the Jaynes-Cummings Hamiltonian in this limit and only considering the computational transmon levels leads to an effective Hamiltonian [Koch2007]

$$\hat{H}_{\text{eff}} = \frac{\hbar\omega_q'}{2}\hat{\sigma}^z + \left(\hbar\omega_r' + \hbar\chi\hat{\sigma}^z\right)\hat{a}^\dagger\hat{a}, \tag{2.6}$$

with the dispersive shift χ. Both the qubit and resonator frequencies are renormalized, as is indicated by the primes. This Hamiltonian can be understood as qubit state dependent resonator frequency shift, i.e., the resonator shifts by 2χ depending on the qubit state. This effect is used to measure the qubit state in a quantum non-demolition measurement (QND) by probing the resonator transmission [Blais2004].

2.1.3 Dispersive Coupling of Two Qubits via Cavity Bus

As emphasized in the introduction, one of the basic blocks for quantum information processing are two-qubit gates. The required qubit-qubit interaction can be achieved, by coupling the two qubits dispersively to a common cavity. This resonator allows for coherent exchange of virtual photons [Blais2004, Blais2007, Majer2007]. The interaction Hamiltonian has the form

$$\hat{H}_{\mathrm{2q,int}} = \hbar J(\hat{\sigma}_1^+\hat{\sigma}_2^- + \hat{\sigma}_1^-\hat{\sigma}_2^+), \qquad J = \frac{g_1 g_2}{2}\left(\frac{1}{\Delta_1} + \frac{1}{\Delta_2}\right) \tag{2.7}$$

with the interaction energy J in terms of the qubit-bus resonator coupling $g_i \coloneqq {g_{01}}^{(i)}$ and detuning from the resonator Δ_i of qubit i [Blais2007]. The qubit excitation and de-excitation operators $\hat{\sigma}^+$ and $\hat{\sigma}^-$ are given by $\hat{\sigma}^\pm = \frac{1}{2}(\hat{\sigma}^x \pm i\hat{\sigma}^y)$. Notably, this 'quantum bus' mediated coupling allows for non-local interactions between distant qubits [Majer2007]. When the qubits are detuned w.r.t to each other with $J \ll |\omega_q, 1-\omega_q, 2|$, the interaction is effectively turned off because in this regime the coupling term is non-energy conserving [Blais2007, Baur2012b]. This allows to turn the interaction dynamically on and off by tuning the individual qubit frequencies.

2.2 Qubit Relaxation and Dephasing

Qubits lose their information due to decay into vacuum and coupling to the noisy environment. Several physical processes lead to decay of the excited qubit state $|1\rangle \to |0\rangle$, so-called amplitude damping. This loss occurring at a rate Γ_1 leads to a finite *qubit relaxation* time $T_1 = 1/\Gamma_1$ [Steffen2013a]. Different decay channels are discussed by Koch *et al.* in [Koch2007], such as Purcell enhanced spontaneous emission, dielectric losses, relaxation due to quasiparticle tunneling and coupling to the flux line. The latter contribution is the one to be considered with respect to flux gates. Inductive coupling of the SQUID loop and the entire transmon circuit to the flux line is estimated in reference [Koch2007] to give an upper bound to the energy relaxation time $T_1 > 20\,\mathrm{ms}$, which is not limiting. On the other hand, capacitive coupling, as discussed by Baur in [Baur2012b] is more relevant as the lower bound to T_1 for this channel calculated with their transmon parameters is $T_1 > 50\,\mu\mathrm{s}$, i.e., as soon as the qubit's T_1 times reach the $50\,\mu\mathrm{s}$ mark, the capacitive coupling has to be considered.
A second type of information loss of pure quantum nature is the so-called decoherence or *dephasing* quantifying the loss of relative phase information between the $|0\rangle$ and $|1\rangle$ states. I.e., when writing the qubit state in terms of Bloch angles θ and ϕ, $|\psi\rangle = \cos(\theta/2)\,|0\rangle + e^{i\phi}\sin(\theta/2)\,|1\rangle$, the pure dephasing time T_ϕ is the time scale on which the angle ϕ gets randomized. Since also amplitude damping leads to a loss of phase information, it is convenient to define the combined dephasing time

$$\frac{1}{T_2} = \frac{1}{2T_1} + \frac{1}{T_\phi} \tag{2.8}$$

which is directly accessible in a Ramsey type measurement. Decoherence originates in fluctuations of the qubit frequency. Different sources of noise causing frequency drifts are discussed by

Koch *et al.* in [Koch2007], such as charge noise, flux noise, critical current noise, E_C noise and dephasing due to quasiparticle tunneling. Again, a critical contribution is the flux noise which comes predominantly from room temperature electronics. Typically the noise power spectrum $S(\omega)$ of electronic noise has a $1/f = 2\pi/\omega$ frequency dependence (see also Appendix A). The coherence time T_2 limited by $1/f$ flux noise is given by [Koch2007]

$$T_2 \approx \frac{1}{A}\left|\frac{\partial\omega_q}{\partial\Phi}\right|^{-1} = \frac{\Phi_0}{A}\frac{2}{\pi\omega_q^{\max}}\frac{1}{\sqrt{\tan(\frac{\pi\Phi}{\Phi_0})\sin(\frac{\pi\Phi}{\Phi_0})}} \qquad S(\omega) = \frac{2\pi A^2}{\omega}, \tag{2.9}$$

where A is the flux noise amplitude at 1 Hz and can be calculated form the noise spectra of the electronic devices such as voltage sources and AWGs.

2.3 Two-Qubit Controlled-Phase Gate

Two qubits that are dispersively coupled via cavity bus exchange their excitation $|01\rangle \rightleftarrows |10\rangle$ coherently at a coupling rate J when being on resonance. On the other hand, the interaction is turned off, if they are far detuned (see section 2.1.3). When tuning the two far off-resonant qubits gradually into resonance, the non-computational level $|20\rangle$ anti-crosses the computational $|11\rangle$ state before reaching the anti-crossing between the $|01\rangle$ and the $|10\rangle$ states due to the negative anharmonicity of the transmons (see Fig. 2.1). This fact can be used, to design a qubit-qubit interaction affecting only the $|11\rangle$ state resulting in a conditional operation. The resonator mediated coupling between these two states is even enhanced by a factor of $\sqrt{2}$ with respect to the coupling J between the excited qubit states $|01\rangle$ and $|10\rangle$ [Koch2007].

Our approach to turn this interaction into a conditional two-qubit gate is based on the scheme first proposed in Ref. [Strauch2003] for flux qubits and later adapted for dispersively coupled transmon qubits [DiCarlo2009, DiCarlo2010]. The two qubits are parked at frequencies $\omega_a^{\text{park}} > \omega_b^{\text{park}}$ such that $\Delta_q = \omega_a^{\text{park}} - \omega_b^{\text{park}} > \alpha$, i.e. the qubit frequency separation is larger then the anharmonicity. This allows to tune the $|1_a 1_b\rangle$ state into resonance with the non-computational $|2_a 0_b\rangle$ state without crossing any other levels (see Fig. 2.1). Interaction with this non-computational state accumulates a conditional phase for the $|11\rangle$ state. The resonance condition for this interaction is $\omega_a(\theta_{\text{CZ}}) - \alpha = \omega_b$. At this point with flux angle $\theta_{\text{CZ}} = \pi\Phi_a/\Phi_0$, the eigenstates of the Hamiltonian are

$$|\pm\rangle = \frac{1}{\sqrt{2}}\left(|20\rangle \pm |11\rangle\right), \tag{2.10}$$

with frequencies $\omega_\pm = \omega_{11} \pm \zeta(\theta_{\text{CZ}}) = \omega_{11} \pm \sqrt{2}J$, where $\omega_{11} = \omega_a + \omega_b$, J is the cavity bus mediated coupling and $\zeta(\theta)$ is the bending of the $|11\rangle$ branch due to the avoided-crossing (compare Fig. 2.1).

There exist different schemes to perform gates at this point. In the *non-adiabatic* scheme, the initial two-qubit state written as a superposition of the four basis states $|00\rangle, |01\rangle, |10\rangle$ and $|11\rangle$ is pulsed instantaneously to the interaction point θ_{CZ}. Only the $|11\rangle$ component experiences the interaction with the non-computational $|20\rangle$ state. This part of the wavefunction can be rewritten as $|11\rangle = 1/\sqrt{2}(|+\rangle - |-\rangle)$ in terms of the eigenfunctions of the interaction Hamiltonian. It evolves as

$$|\psi(t)\rangle = \frac{1}{\sqrt{2}}e^{-i\omega_+ t}\left(|+\rangle - e^{-i\delta t}|-\rangle\right), \tag{2.11}$$

where $\delta = \omega_- - \omega_+ = 2\zeta(\theta_{\mathrm{CZ}}) = 2\sqrt{2}J$, i.e., the population oscillates between the $|11\rangle$ and the $|20\rangle$ states. After the time $\tau = 2\pi/\delta = 2\pi/(2\sqrt{2}J)$, all the population will be back in the initial state while having collected the conditional phase $\phi_c = -i\pi$ and the dynamical phase

$$\phi_d = -i\left(\omega_{11}(\theta) - \omega_a^{\mathrm{park}} - \omega_b^{\mathrm{park}}\right)\tau. \tag{2.12}$$

In the *adiabatic* scheme, the system is tuned to the interaction point adiabatically with respect to the $|11\rangle \leftrightarrow |20\rangle$ avoided crossing, such that the non-computational state $|20\rangle$ is never populated. This way, the conditional phase acquired is expressed as $\phi_c = -\int \zeta\left(\theta(t)\right) \mathrm{d}t$, allowing for arbitrary phase gates [DiCarlo2009]. On the downside, adiabatic operation requires longer gate times. An optimal analytic flux pulse shape for fast adiabatic gates was proposed in [Martinis2014a] minimizing the gate time of the adiabatic gate.

In both cases, tuning qubit q_a to this interaction for a specific time, evolves the simplified two-level system in general under the unitary transformation [DiCarlo2009]

$$\widehat{U} = \begin{pmatrix} 1 & 0 & 0 & 0 \\ 0 & e^{i\phi_{01}} & 0 & 0 \\ 0 & 0 & e^{i\phi_{10}} & 0 \\ 0 & 0 & 0 & e^{i\phi_{11}} \end{pmatrix} \tag{2.13}$$

where ϕ_{10} and ϕ_{01} are the dynamically acquired phases of qubits q_a and q_b, respectively and $\phi_{11} = \phi_{10} + \phi_{01} + \phi_c$ contains the conditional phase. In a rotating frame rotating at the qubit Larmor frequency, the dynamical phases can be expressed as $\phi_{ab} = \int \delta\omega_{ab}(t)\mathrm{d}t$ with frequency deviation $\delta\omega_{ab}(t) = \omega_{ab}^{\mathrm{park}} - \omega_{ab}(t)$ caused by the flux pulse. Despite pulsing only qubit q_a, ϕ_{01} is also non-zero due to finite flux cross-talk. The dynamical phases can be measured an corrected

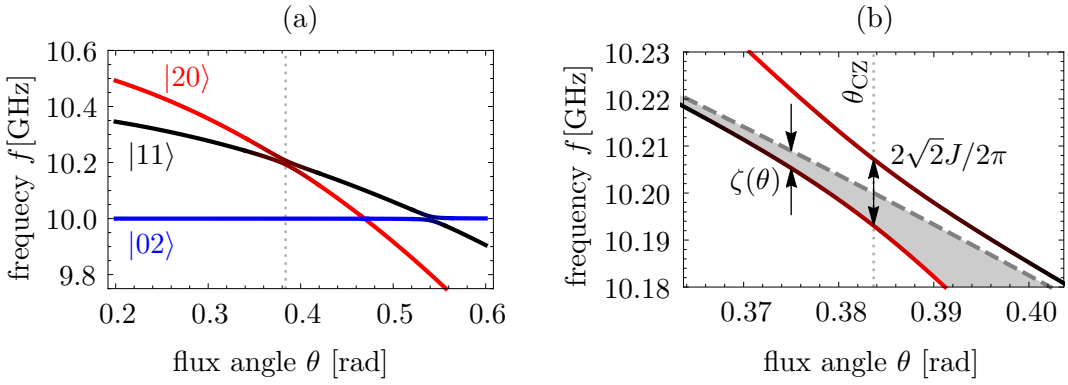

Fig. 2.1: (a) Simulated level structure of two coupled transmons q_a and q_b ($\omega_a = 2\pi \times 5.4\,\mathrm{GHz}$, $\omega_b = 2\pi \times 5.0\,\mathrm{GHz}$, $\alpha = 2\pi \times 200\,\mathrm{MHz}$) as a function of the flux angle $\theta = \pi\Phi_a/\Phi_0$ of qubit q_a. (b) Zoom-in to the relevant anti-crossing between the computational state $|11\rangle$ and the non-computational state $|20\rangle$ with spacing $2\sqrt{2}J/2\pi$. The dotted line marks the interaction angle for a C-Phase gate. ζ quantifies the frequency shift of the lower branch due to the avoided crossing with the $|20\rangle$ level.

by zero-time virtual-Z gates [McKay2017] leading to the unitary transformation

$$\widehat{U}_{\mathrm{CZ}} = \begin{pmatrix} 1 & 0 & 0 & 0 \\ 0 & 1 & 0 & 0 \\ 0 & 0 & 1 & 0 \\ 0 & 0 & 0 & -1 \end{pmatrix} \tag{2.14}$$

in the computational basis. The two-qubit C-Phase gate (also CZ gate) can be used in combination with two Hadamard gates H to build a controlled-NOT gate (CNOT):

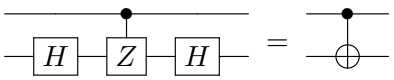

$$H = \frac{1}{\sqrt{2}} \begin{pmatrix} 1 & 1 \\ 1 & -1 \end{pmatrix}. \tag{2.15}$$

On-Off Ratio

In a design for a conservative two-qubit gate time $t_{2\mathrm{qb}} = 90\,\mathrm{ns}$ with anharmonicity $\alpha = 240\,\mathrm{MHz}$ for all qubits and coupling resonator detuning $\Delta_a \approx 2\pi \times 1.9\,\mathrm{GHz}$ and $\Delta_b = 2\pi \times 1.5\,\mathrm{GHz}$ for qubit q_a and q_b, respectively, the qubit-resonator coupling is calculated to be around $g_a \approx 78\,\mathrm{MHz}$ and $g_b \approx 90\,\mathrm{MHz}$. This leads to a residual interaction at the parking positions [DiCarlo2009]

$$\zeta_{\mathrm{park}} \approx -2g_a^2 g_b^2 \left(\frac{1}{\Delta_a \Delta_b^2} + \frac{1}{\Delta_a^2 \Delta_b} \right) \approx 40\,\mathrm{kHz}. \tag{2.16}$$

This is already 1 % of the designed qubit-qubit coupling $J/2\pi = 4\,\mathrm{MHz}$. For faster gate times, i.e. larger J and thus larger g's, this trade-off between cross-talk and gate speed gets problematic. Then the residual interaction can not be neglected anymore and the identity gate gets non-trivial.

2.3.1 Gate Fidelity and Adiabaticity

To surpass the error correction threshold, it is a vital to reach gate fidelities above 99 % even for very robust QEC codes [Versluis2017]. A cause of infidelity of the non-adiabatic C-Phase gate as described above, is leakage due to imperfect flux pulse shapes into the $|20\rangle$, i.e., incomplete recovery of the population that was transferred into this non-computational state during the gate. In theory this non-adiabatic gate scheme is modeled with a perfect square pulse, which is very hard to accomplish, since it contains infinite frequency components. Simulations in Ref. [Ghosh2013] based on realistic parameters (300 MHz anharmonicity qubits) show that it is possible to get 99.99 % fidelity CZ-gates with a simple pulse profile that contains only low frequency parts. The pulse shape that they use for their calculations is an error function-shaped pulse, i.e., a square pulse filtered by a Gaussian filter with width σ. For fixed σ this pulse is also parametrized by only two parameters, pulse height and length, like the square pulse. This work shows, that it is not required to operate purely non-adiabatic to reach high fidelity gates.
Ref. [Martinis2014a] follows a different approach optimizing the adiabatic gate scheme. During the longer adiabatic flux pulse, the qubit leaves its sweet spot and is sensitive to $1/f$ flux noise. Consequently, in this paper they engineer a pulse shape that minimizes the pulse duration under the constraint to stay adiabatic. Using optimal windowing theory, they propose a near optimum solution, expressed as Fourier expansion, whose coefficients can be optimized in situ at the experiment. This pulse shapes were first implemented in reference [Barends2014] achieving a CZ gate fidelity of 99.4 % in $t_g = 43\,\mathrm{ns}$.
Independent of the choice of the analytic pulse shape, any gate optimization that requires to

measure the gate fidelity is potentially time consuming. Especially for the characterization of the fast dynamics of the flux pulse, many free parameters are available in form of a FIR filter (see next chapter) that can be optimized. For this reason, it is preferable to extract all available information on the pulse distortions in the signal chain and calculate predistortion filters inversely compensating for distortions.

Chapter 3

Flux Pulse Predistortion

In this chapter, I first give a brief introduction to linear digital filters. Along the way, a procedure of how to obtain optimal predistortion filters is developed. These filters compensate in advance for distortions which the flux pulse suffers from due to imperfect signal generation and frequency dependent attenuation in the signal chain. Due to the linearity of the filters, they can be applied independent of the optimal analytic flux pulse shape. I.e., they can be applied for both the non-adiabatic pulse scheme proposed in Ref. [Strauch2003, Ghosh2013] and the fast adiabatic gate in Ref. [Martinis2014a]. They correct for signal distortions specific to the setup which can be characterized to some degree by measuring the transfer function of the signal chain. Complementary, the optimization of a few free parameters describing the analytic form of the pulse is done separately by measuring the gate fidelity directly on the sample [Kelly2014].

In particular, we aim to implement infinite impulse response (IIR) filters better suited to correct for effects on a slow timescale. These filter fit our needs very well, since they can be implemented as real time filters on the signal generator and offer a means of compensation for high-pass filters. In particular, when using a bias-T in the signal chain that reduces electronic $1/f$ noise from the arbitrary waveform generator (AWG), the transient response of a flux pulse shows exponentially decaying tails on the order of a few microseconds [Johnson2011PhD, Kelly2014]. This is much longer than the gate time $t_g \approx 100\,\text{ns}$ itself and has influences on consequent flux gates (gate bleed-through). Thus, for a scalable C-Phase gate it is essential to have precise control of the magnetic flux especially after the gate. In this regard, we show that the signal distortions caused by a bias-T can be efficiently inverted with an IIR filter.

Finally, the filter extraction procedure is shown at a data set measured on the warm setup. This proves the capability to inversely compensate distortions on different time scales.

3.1 Estimated Precision Requirement

During a C-Phase gate a flux pulse with pulse length t_g is applied to the control qubit. If the flux pulse has not yet decayed fully before applying a subsequent gate, the qubit acquires an additional phase $\Delta\phi = \Delta\omega_q t_g = 2\pi\Delta f t_g$ due to residual detuning Δf caused by the previous flux pulse. Expressing $\Delta\phi$ in terms of the residual flux pulse offset voltage ΔV leads to

$$\frac{\Delta\phi}{2\pi} = \frac{\partial f}{\partial \Phi}\frac{\partial \Phi}{\partial V}\Delta V t_g. \tag{3.1}$$

With the experimental value for $\partial V/\partial\Phi \approx 5\,\mathrm{V}/\Phi_0$, a gate time $t_g = 100\,\mathrm{ns}$ and the maximum qubit frequency $f_{\max} = 6\,\mathrm{GHz}$ we get

$$\Delta\phi/2\pi \approx 10^2 \Delta V/1\,\mathrm{V}. \tag{3.2}$$

Hence, for maximum phase error of 1 %, the voltage needs to be precisely controlled on the $\Delta V = 0.1\,\mathrm{mV}$ level. For the AWG this requires a precision of $\Delta V/V_{\mathrm{pp}} \approx 2 \times 10^{-5}$ and thus at least 16-bit waveform resolution. In addition, our filters must also be able to compensate distortions on the same order.

3.2 Inverse Filtering: An Excursion to Digital Signal Processing

Inverse filtering is a problem, often encountered in signal processing, as for example in image restoration [Katsaggelos2012] and sound engineering [Havelock2008] where is also called pulse preconditioning by predistortion filters. Here I introduce the signal processing background used to calculate an inverse filter.

3.2.1 Impulse Response

For a linear time-invariant system (LTI system) the *impulse response* $h(t)$ encodes all information to model the response $y(t)$ to an arbitrary input signal $x(t)$. The impulse response is the system response to a Dirac delta impulse $\delta(t)$. Due to linearity, the response to an arbitrary input signal $x(t)$ is uniquely determined by convolution with the impulse response function

$$x(t) = \delta(t) * x(t) \to y(t) = h(t) * x(t), \tag{3.3}$$

where $*$ denotes convolution: $(x_1 * x_2)(t) \coloneqq \int_{-\infty}^{\infty} x_1(\tau) x_2(t-\tau)\,\mathrm{d}\tau$. This can be seen by decomposing $x(t)$ into an infinite sum of delta impulses $x(t) = \delta(t) * x(t)$. Convolution in the time domain corresponds to multiplication in Fourier space:

$$\widehat{y}(f) = \widehat{h}(f)\,\widehat{x}(f), \tag{3.4}$$

where $\widehat{x}(f) = \mathcal{F}[x(t)](f) = \int_{-\infty}^{\infty} x(t) e^{-i2\pi f t}\,\mathrm{d}t$ denotes the Fourier transform from time domain with time variable t to frequency domain in frequency variable f. In other words, an LTI system with impulse response $h(t)$ acts as linear filter with frequency response $\widehat{h}(f)$, also called transfer function.

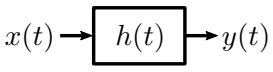

Fig. 3.1: The system response of a LTI system is determined by the impulse response.

Measuring the Impulse Response

In general it is no trivial task to measure the impulse response since it is not possible to generate a ideal Dirac delta impulse which would contain an infinite amount of energy to probe the system at all frequencies. Different methods exist to approximate the impulse response, such as sweeping a sine signal, applying white noise or an MLS signal (maximum length sequence, pseudo-random

noise) etc. [Havelock2008, Stan2002]. A simple, almost direct method is the measurement of a step response $y_u(t) = h(t) * u(t)$ where $u(t)$ denotes the unit step function. According to

$$\frac{d}{dt}y_u(t) = \frac{d}{dt}(h * u)(t) = \int_{-\infty}^{\infty} h(\tau)\frac{d}{dt}u(t-\tau)\,\mathrm{d}t = h(t) * \delta(t) = h(t) \tag{3.5}$$

the impulse response is obtained by derivation of the step response as, e.g., also used in Ref. [Johnson2011PhD]. In contrast to an impulse function, a step function is in general better reproduced on an AWG as it has finite bandwidth (the power spectral density of a step function falls off like $|\widehat{u}(f)| \propto 1/f$). Hence the AWG can reproduce it better than an ideal delta pulse with flat frequency response which would require to put a high amount of energy in the very short pulse. In the context of our application, however, it is not simply possible, to measure the step response of the whole signal chain including the connector to the sample and the frequency response of the sample itself. With an fast oscilloscope, we are only able to measure the cabling down to the sample connector on the warm setup. In a later approach, we also measure the response directly on the qubit in the cold setup as described in section 4.4.

3.2.2 FIR filters

Digital finite impulse response (FIR) filters are linear, non-recursive filters. I.e., they act on a time-discrete sequence using only current and past input samples [Lyons1996]. An FIR filter with the N filter coefficients $h[n], n = 0, 1, ..., N-1$ acts on the digital data set $x[n]$ such that the output sequence is $y[n] = h[n] * x[n]$, where the $*$ hereby indicates discrete convolution.

$$y[n] = h[n] * x[n] = \sum_{k=0}^{N-1} h[k]x[n-k]. \tag{3.6}$$

Often the data set $x[n] = x(nT_s)$ is sampled from a continuous time signal $x(t)$ with sampling frequency $f_s = 1/T_s$ as in the case where $x[n]$ is the trace of an oscilloscope with sampling rate f_s. The impulse response of an FIR filter corresponds to the filter coefficients $h[n]$, hence the name finite impulse response filter as the number of filter coefficients N, also called filter taps, is finite. Commonly used filters like moving average filters, Gaussian filters, etc. are usually realized as FIR filters [Lyons1996, Smith1997]. In Fig. 3.2 a simple example of the application of an FIR filter (5-tap moving average) to a step function $x[n]$ is depicted. The effect of the FIR filter vanishes after at most N samples, i.e., after the time NT_s (compare Fig. 3.2 (b)), again indicating the finiteness of FIR filters.

As we want to use our filters for the preconditioning of pulses played on demand in real time, it is important to keep the numbers of filter taps on a reasonable small order, such that $NT_s \sim T_p$, where T_p is the pulse length. Thus we can apply the FIR filter offline and replay predistorted patterns with the waveform generator. Applying FIR filters on the fly is computationally demanding since it involves many multiplications and introduces a long delay $\sim NT_s$ [Lyons1996].
For distortions on a much longer time scale, e.g., on the order of the repetition period of subsequent pulses T_r like the high-pass effect of a bias-T, FIR filters are not suitable for real time assembled waveforms. However, we still need to apply filters compensating for these effects. This can be done using another class of filters, so-called IIR filters (discussed below in section 3.2.4). These filters are much better suited for real time filtering of slow distortions with an

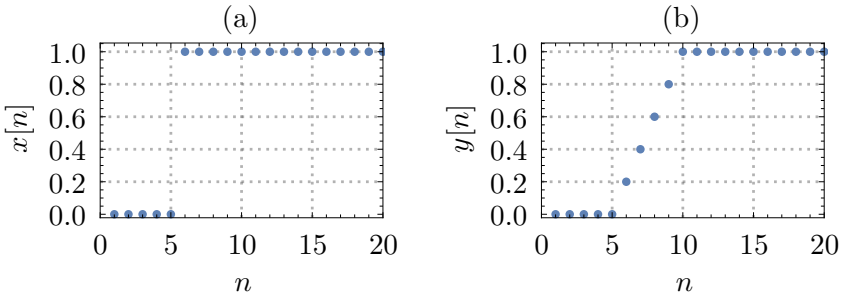

Fig. 3.2: Example of an FIR 5-tap filter (moving average, $h[n] = 0.2, n = 1, ..., 5$). (a) input signal $x[n]$. (b) filtered sequence $y[n] = h[n] * x[n]$.

analytic description. In combination with IIR filters the required number FIR filter taps can be kept small, such that the FIR filter can be applied offline correcting fast ripples and only the IIR filters are implemented in real time compensating for slow decaying distortions.

3.2.3 Inversion of FIR Filters

For the pulse pre-conditioning, or pulse shaping, we want to invert the effect of the system transfer function, i.e., the impulse response. This is no trivial task, since the impulse response function $h(t)$ for physical systems typically acts as a low-pass filter. Hence, an inverse impulse response filter $h_{\text{inv}}(t)$ defined by $h(t) * h_{\text{inv}}(t) = \delta(t)$ is a high-pass filter. This can be seen directly in the Fourier domain, where

$$\widehat{h}(f)\widehat{h}_{\text{inv}}(f) = \widehat{\delta}(f) = 1 \qquad \Longrightarrow \qquad \widehat{h}_{\text{inv}}(f) = \frac{1}{\widehat{h}(f)}. \tag{3.7}$$

This is problematic because the inversion of the filter kernel dramatically amplifies high frequency noise present in the measured impulse response. For $f \gg f_c$, where f_c specifies the cutoff frequency of the transfer function $\widehat{h}(f)$, typically $\widehat{h}(f) \ll 1$ such that for noisy data $\widehat{h}_{\text{inv}}(f) = 1/(\widehat{h}(f) + \widehat{n}(f))$ is dominated by the noise $n(t)$ for high frequencies.

L_2 Total Variance Regularization

Amplified high frequency noise is a problem generally present in deconvolution of measurement data. To overcome this issue, mainly in the realm of image processing, various deconvolution algorithms were developed, e.g. Wiener deconvolution [Dhawan1985], Richardson-Lucy deconvolution [Lucy1974, Richardson1972] and the nonlinear total variation based noise removal algorithm in [Rudin1992]. From a mathematical viewpoint, deconvolution of noisy data is an ill-posed problem:

$$y = h * x + n \iff \mathbf{y} = H\mathbf{x} + \mathbf{n}, \tag{3.8}$$

where x is the unknown variable and the measured signal y effected by the noise n. In our case, the convolution kernel is also a measured quantity suffering from noise. Alternatively, the convolution can also be written as vector matrix multiplication with the convolution matrix H and the signals written as column vectors $\mathbf{x}$, $\mathbf{y}$ and $\mathbf{n}$. As described above, straight forward inversion of H results in very bad approximations for the deconvolved signal $\mathbf{x}$, since the matrix H has very small eigenvalues amplifying the noise n dramatically when being inverted. To solve

such ill-posed problems, typically a regularization method is applied (e.g. Tikhonov regularization [Tikhonov1963]):

$$\tilde{\mathbf{x}} = \underset{\mathbf{x}}{\operatorname{argmin}}\{\|H\mathbf{x} - \mathbf{y}\|_2^2 \ + \alpha R(\mathbf{x})\}, \tag{3.9}$$

where $R(\mathbf{x})$ is called regularizer and $\|\mathbf{x}\|_2^2$ denotes the L_2 norm. The regularizer $R(\mathbf{x})$ introduces a penalty on solutions with large $R(\mathbf{x})$, i.e., it gives preference to solutions with desirable properties defined through $R(\mathbf{x})$[1]. The parameter α defines the weight of the regularization term. We use a total variation method, adapted from the total variation deconvolution described in [Rudin1992] with the L_2 total variation regularizer $R(\mathbf{x}) = \|D\mathbf{x}\|_2^2 = \sum_{n=1}^{N-1}(x_n - x_{n-1})^2$. D can be written as $N-1 \times N$ matrix:

$$D\mathbf{x} = \begin{pmatrix} 1 & -1 & 0 & \cdots & 0 \\ 0 & 1 & -1 & \cdots & 0 \\ \vdots & & \ddots & & \vdots \\ 0 & \cdots & & 1 & -1 \end{pmatrix} \begin{pmatrix} x_0 \\ x_1 \\ \vdots \\ x_{N-1} \end{pmatrix} = \begin{pmatrix} x_0 - x_1 \\ x_1 - x_2 \\ \vdots \\ x_{N-1} - x_{N-2} \end{pmatrix}. \tag{3.10}$$

With the L_2 norm, the solution can be calculated very efficiently with a linear least squares solver when rewriting the problem as

$$\begin{aligned} \tilde{\mathbf{x}} &= \underset{\mathbf{x}}{\operatorname{argmin}}\{\|H\mathbf{x} - \mathbf{y}\|_2^2 + \alpha R(\mathbf{x})\} && (3.11)\\ &= \underset{\mathbf{x}}{\operatorname{argmin}}\{\|H\mathbf{x} - \mathbf{y}\|_2^2 + \alpha\|D\mathbf{x}\|_2^2\} && (3.12)\\ &= \underset{\mathbf{x}}{\operatorname{argmin}}\left\{\left\|\begin{pmatrix} H\mathbf{x} - \mathbf{y} \\ \sqrt{\alpha}D\mathbf{x} \end{pmatrix}\right\|_2^2\right\} && (3.13)\\ &= \underset{\mathbf{x}}{\operatorname{argmin}}\{\|(H, \sqrt{\alpha}D)^T\mathbf{x} - (\mathbf{y}, 0)^T\|_2^2\}. && (3.14) \end{aligned}$$

The total variation regularizer $R(\mathbf{x})$ introduces a penalty on abrupt variations in $\mathbf{x}$, hence it reduces noise in $\mathbf{x}$. The larger the chosen regularization parameter α, the smoother is the solution $\mathbf{x}$.

Applied to the problem of calculating the inverse FIR filter, we define $x_n = x(nT_s)$ of length N to be the input sequence to the AWG, and $y_k = y(kT_{\text{osc}})$ with length M to be the signal measured on an oscilloscope with sampling rate $f_{\text{osc}} = 1/T_{\text{osc}}$. Further, let $H = H_{\text{imp}}H_{\text{res}}$ be the impulse response matrix. H_{imp} is a $M \times M$ matrix performing the convolution with the measured impulse response and H_{res} is a $N \times M$ resampling matrix, resampling from the AWG sampling rate to the oscilloscope sampling rate. Solving the regularized matrix equation Eq. 3.14 for $\mathbf{x}$ with $\mathbf{y}_\delta = (0, 0, ..., 0, 1, 0, ..., 0)$ with a linear least squares solver, yields the inverted impulse response

$$\mathbf{h}_{\text{inv}} = \underset{\mathbf{x}}{\operatorname{argmin}}\{\|(H_{\text{imp}}H_{\text{res}}, \sqrt{\alpha}D)^T\mathbf{x} - (\mathbf{y}_\delta, 0)^T\|_2^2\}. \tag{3.15}$$

This solution $\mathbf{h}_{\text{inv}}$ corresponds directly to the wanted inverse FIR filter.

3.2.4 IIR filters

Infinite impulse response filters are another class of linear digital filters that can have, as the name states, infinite response to an impulse. IIR filters can be seen as FIR filters with additional

[1] For the Tikhonov regularization, often $R(\mathbf{x}) = \|\mathbf{x}\|_2^2$ is chosen, leading to solutions $\tilde{\mathbf{x}}$ with a small norm.

feedback coefficients. Formally, the n-th output of an input sequence $x[i]$ is calculated as

$$y[n] = \sum_{i=0}^{N} b[i]x[n-i] + \sum_{i=1}^{M} a[i]y[n-i] \tag{3.16}$$

where N is the feedforward filter order, $b[i]$ the feedforward filter coefficients (FIR part) and M is the feedback filter order with the feedback filter coefficients $a[i]$ (purely IIR part). In Fig. 3.3 an example of a simple first-order IIR filter applied to a step function (a) is shown. Despite the filter having only two coefficients ($a[1] = 0.6, b[0] = 0.4$), its effect lasts very long (limited only due to finite resolution of the numbers $y[n]$). This class of filters is well suited to model an analog filter, as shown in the following sections. Especially, the slowly decaying exponential distortions, caused by high-pass filters as for example the bias-T, reflections and the skin effect [Barends2014, Kelly2014] can be corrected with IIR filters, which makes them even more interesting for our purpose. In the following, I will go through some mathematical tools to characterize IIR filters.

z-Transform

In electronics the Laplace transform is an important tool to investigate the spectral properties of continuous signals and solve differential equations:

$$H(s) = \mathcal{L}[h(t)](s) \coloneqq \int_0^\infty h(t)e^{-st}\,\mathrm{d}t, \qquad s \in \mathbb{C}. \tag{3.17}$$

This is very similar to the Fourier transform, however expanding the class of functions that can be transformed. Its time discrete version is the z-Transform. It is defined as

$$H(z) = \mathcal{Z}[h(n)](z) = \sum_{n=-\infty}^{\infty} h[n]z^{-n} \tag{3.18}$$

where $z \in \mathbb{C}$ is a complex variable. In the z-domain we can express the discrete time transfer function $H(z)$ of an IIR filter by

$$H(z) = \frac{Y(z)}{X(z)} = \frac{\sum_{n=0}^{N} b[n]z^{-n}}{1 - \sum_{n=1}^{M} a[n]z^{-n}} \tag{3.19}$$

(derivation e.g in [Lyons1996]). In the special case $z = e^{i\omega}$, $\omega \in \mathbb{R}$, the transfer function corresponds to the discrete time Fourier transform of the impulse response. I.e., the unit circle in the complex z-plane corresponds to the the frequency response of the IIR filter $|H(\omega)| = |H(z = e^{i\omega})|$.

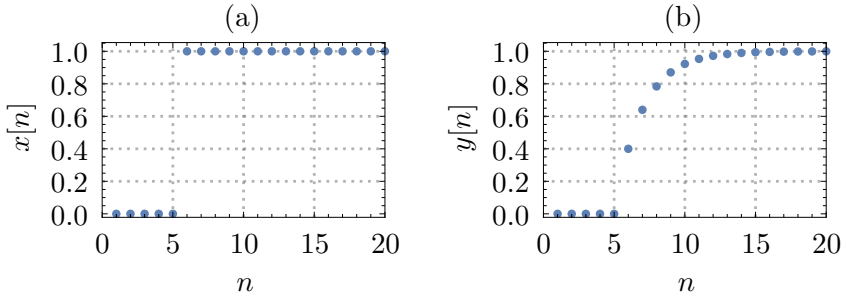

Fig. 3.3: Example of a first-order IIR filter with filter coefficients $a[1] = 0.6, b[0] = 0.4$.

IIR Filter Design: Bilinear Transform

There exist different design techniques for IIR filters adapted for various applications (e.g. impulse invariance methods described in [Lyons1996]). A straightforward method to get a discrete filter approximating a continuous Laplace transfer function $H_L(s)$ is the *bilinear transform* [Lyons1996]. Substituting s in $H_L(s)$ for

$$s \mapsto s(z)\frac{2}{T_s}\left(\frac{1-z^{-1}}{1+z^{-1}}\right) \tag{3.20}$$

yields the transfer function in the z-domain $H(z) = H_L(s(z))$. The bilinear transform suffers of so-called frequency warping, i.e., non-linear frequency shifts of features in the spectrum close to the Nyquist frequency (half the sampling frequency) [Lyons1996]. However, as we only want to correct for slow distortions, this will not affect us.

Stability

A critical characteristic of IIR filters is their stability. A filter is called stable, if its response to any finite signal stays finite, too. When analyzing IIR filters in the z-domain, the stability of the filter can immediately be inferred by rewriting the transfer function $H(z)$ in Eq. 3.19 as

$$H(z) = \frac{(z-z_0)(z-z_1)...(z-z_N)}{(z-p_0)(z-p_1)...(z-p_M)} \tag{3.21}$$

$$= \sum_k \frac{A_k}{z-p_k}, \tag{3.22}$$

where z_k are the zeros and p_k the poles of $H(z)$. If all the poles lie inside the unit circle, the filter is stable (poles outside the unit circle have an exponentially growing impulse response) [Lyons1996]. Hence, the inverse of an IIR filter $H_{inv}(z) = 1/H(z)$ is stable, if all zeros of $H(z)$ are inside the unit circle ($|z_k| < 1$). This is not necessarily guaranteed and has to be taken care of.
The form 3.22 is obtained by partial fraction expansion showing that any IIR filter can by expressed as a sum of single-pole filters with individual gain A_k.

IIR Fitting

For any analog RLC 4-port circuit the complex transmission $V_{\text{out}}(s)/V_{\text{in}}(s)$ in the Laplace domain can be written down straightforwardly using Kirchhoff's current and voltage law and the complex impedances of a resistor, an inductance and a capacitor being $Z_R = R$, $Z_L = sL$ and $Z_C = 1/sC$, respectively. A digital approximation in form of an IIR filter is obtained by performing the bilinear transform. Any transfer function of the form 3.19 can be rewritten as a sum of first order or so-called single-pole filters (see Eq. 3.22) [Lyons1996]. Such a single-pole filter corresponds to a pole in the complex transfer function representing a capacitive or inductive element. Pure RC and RL poles are on the real axis. In the time domain, the step response of one of these poles have the general exponential form

$$f(t) = (A + Be^{-t/\tau})u(t), \tag{3.23}$$

that can be fitted to measurement data ($u(t)$ is the Heaviside function). This fitting model is well suited in a sense, that its corresponding IIR filter is invertible. The Laplace transform of this step response function is

$$F(s) = \frac{A}{s} + \frac{B\tau}{1+s\tau}. \tag{3.24}$$

The impulse response $h(t) = \frac{d}{dt}f(t)$ is easily obtained in the Laplace domain by

$$H(s) = \mathcal{L}[h(t)](s) = \mathcal{L}\left[\frac{d}{dt}f(t)\right](s) = sF(s) = s\left(\frac{A}{s} + \frac{B\tau}{1+s\tau}\right). \tag{3.25}$$

Inverting this impulse response function, we get

$$H_{inv}(s) = \frac{1}{H(s)} = \frac{1+s\tau}{A+s\tau(A+B)}. \tag{3.26}$$

By bilinear transform the coefficients of the IIR filter correcting for the effect described by Eq. 3.23 can be extracted. This IIR filter is a first-order filter with three coefficients a_1, b_0 and b_1 with the transfer function

$$H_{\text{model}}(z) = \frac{b_0 + b_1 z^{-1}}{1 - a_1 z^{-1}}. \tag{3.27}$$

Expressed with the parameters from model 3.23, the filter coefficients are given by $a_1 = (A\tau + 2B\tau - AT_s)/\lambda$, $b_0 = (2\tau + T_s)/\lambda$ and $b_1 = (-2\tau + T_s)/\lambda$, where $\lambda = 2A\tau + 2B\tau + AT_s$ and T_s is the sampling period. This result implies, that the behavior of simple RC and LC circuits can be modeled and inverted by a first order IIR filter. Multiple poles can be separated well, if their characteristic decay times τ are different, then the exponentials can be fitted independently to extract the corresponding inverse IIR filter coefficients.

3.3 Digitally Inverting a Bias-T

A bias-T is a commercially available microwave component for combining a low frequency signal applied to the DC port with a high frequency signal on the RF port (for the port assignment see the circuit diagram in Fig. 3.4). Signals applied to the DC port, usually a bias voltage, are low pass filtered whereas the RF port acts as RC high-pass filter, allowing only high frequency signals to pass. We use a bias-T in our setup to set the flux bias voltage for our transmon qubits and use the RF port to apply fast flux pulses generated on an AWG. In addition, the high-pass properties of the RF input port filters the low frequency part of the electronic $1/f$ noise from the AWG. This has direct influence on the dephasing time of the qubits (see section 2.2).

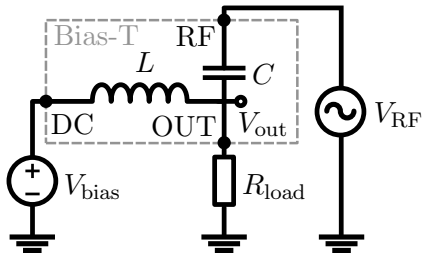

Fig. 3.4: Simplified circuit of a bias-T. The RF port is capacitively coupled to the OUT port. The DC port is used to feed-in a bias voltage. R_{load} represents the flux line in our setup with $50\,\Omega$ impedance, V_{bias} stands for the DC voltage source and V_{RF} for the voltage from the AWG.

3.3.1 First Order High-Pass Filter: A Simplified Bias-T

A filter is characterized by its frequency response. While a low-pass filter lets DC and oscillating signals up to a characteristic cutoff frequency f_c pass, an ideal high-pass filter blocks those components and only lets signals with frequency higher than f_c pass (sometimes also called sinc or brick-wall filter). In practice the frequency response of filters are never rectangular shaped but rather smooth curves and usually the 3dB point is stated as the cutoff frequency (see Fig. 3.5 for the example of a realistic high-pass filter). When neglecting the DC port of a bias-T, i.e., assuming infinite internal impedance of the DC voltage source, the capacitance together with the load act as analog RC first-order high-pass filter on signals applied to the RF input port. Its transfer function is plotted in Fig. 3.5 assuming realistic parameters. The effect of such a simplified bias-T on a pulse train is depicted in Fig. 3.6. The transfer function of this filter, sometimes also referred to as DC-block, is

$$H(s) = \frac{V_{\text{out}}(s)}{V_{\text{in}}(s)} = \frac{V_{\text{out}}(s)}{V_{RF}(s)} = \frac{sR_{\text{load}}C}{1 + sR_{\text{load}}C} \tag{3.28}$$

in the Laplace domain, where V_{RF} is the input voltage and V_{out} is the output voltage (voltage seen by the load). For such a filter the cutoff frequency f_c is given by $f_c = 1/(2\pi\tau_{RC})$, where $\tau_{RC} = R_{\text{load}}C$ is the time scale of charging the capacitor. The impulse response of this filter is

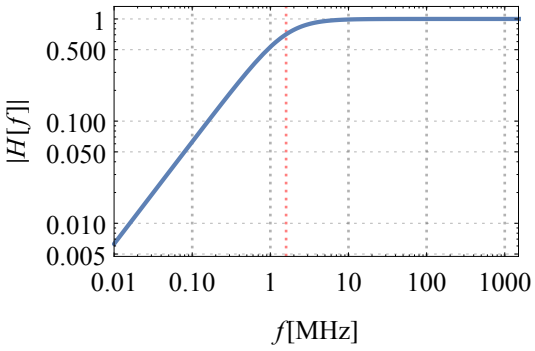

Fig. 3.5: Frequency response of a RC high-pass filter with $R = R_{\text{load}} = 50\,\Omega$, $C = 2\,\text{nF}$. The red dotted line marks the filters cutoff frequency $f_c = 1.59\,\text{MHz}$.

the inverse Laplace transform of $H(s)$:

$$h(t) = \mathcal{L}[H(s)](t) = \delta(t) - \frac{1}{\tau_{RC}} e^{-t/\tau_{RC}} u(t), \tag{3.29}$$

where $\delta(t)$ is the Dirac delta function and $u(t)$ is the unit step function (Heaviside function). For LTI systems, we get the system response to an arbitrary pulse by convolving with the impulse response. E.g., for a rectangular pulse train the transient response looks as as depicted in Fig. 3.6 (b). To invert the effect of this simplified bias-T, the transfer function $H(s)$ in Eq. 3.28 is rewritten into the form 3.25 with parameters $A = 0, B = 1$ and $\tau = R_{\text{load}}C$. I.e., our IIR inversion model is directly applicable to this bias-T simplification and the predistortion IIR filter coefficients can calculated according to Eq. 3.27. The effect of the inverse IIR filter and the system response to the pre-conditioned pulse pattern are shown in Fig. 3.7.

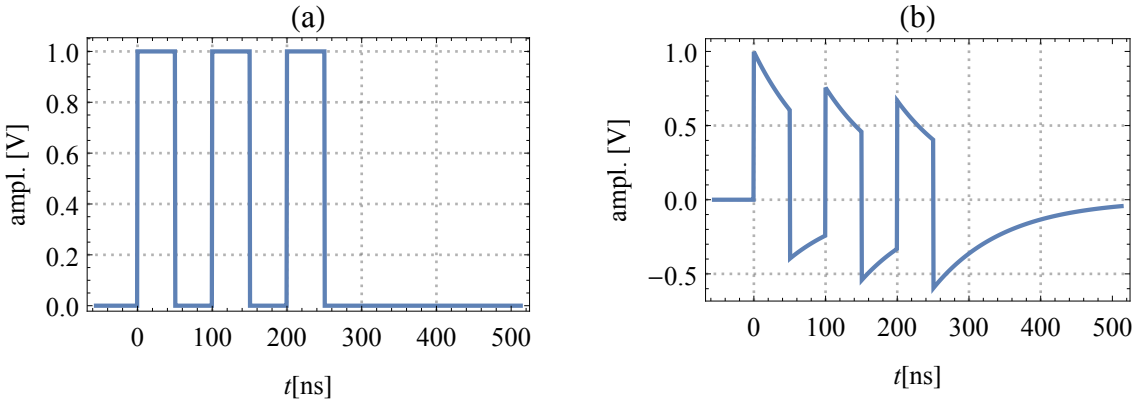

Fig. 3.6: (a) A pulse train consisting of three consecutive 50 ns square pulses. (b) Simulated system response of the high-pass filter to the pulse train.

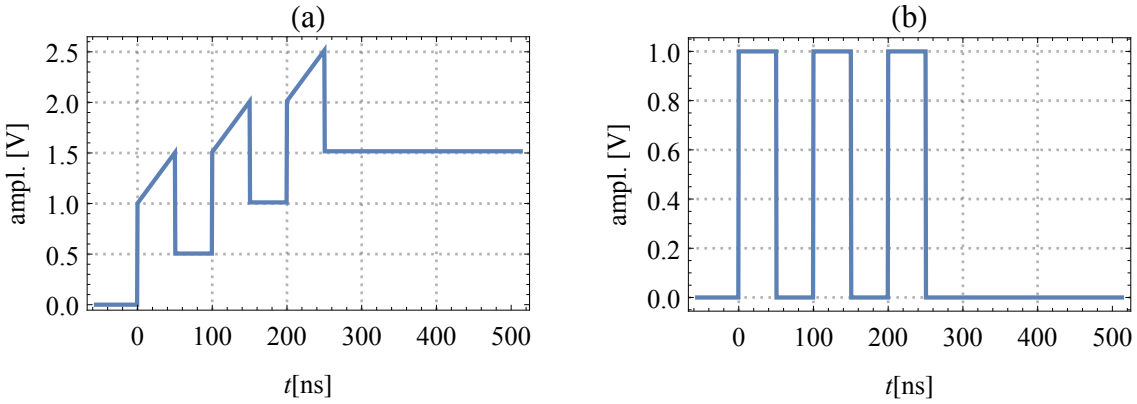

Fig. 3.7: (a) Predistorted pulse train with the inverse IIR filter. (b) Simulated system response to the inverse filtered pulse train.

3.3.2 The Out-Of-Range Problem

The capacitor in the bias-T charges when a flux pulse is applied, and would immediately start to discharge as soon as the rectangular flux pulse has finished, inducing a opposite current through the flux line (compare also Fig. 3.6(b)). As we want to omit this effect, the charge on the capacitor needs to be held by an constant voltage offset. This corresponds to the offset after the shaped pulse train in Fig. 3.7 (a), which plots the AWG output voltage to be applied when correcting for the bias-T distortion. Obviously, after a few pulses, the AWG output range will be exceeded. More quantitatively, the additive offset after a pulse is $V_{\text{offset}} = V_{\text{pulse}} T_{\text{pulse}}/\tau$, where V_{pulse} is the amplitude and T_{pulse} the length of the flux pulse. I.e., for a pulse amplitude of half of the maximal output voltage of the AWG, the maximal total length of all flux pulses without discharging the capacitor of the bias-T is 2τ. Connecting the RF and OUT port of the bias-T with a high-impedance resistor for a slow discharge changes the behavior of the high-pass filter such that it does not attenuate the low-frequency noise sufficiently anymore (see Appendix B.2). A possible solution to this issue could be weak interleaved compensation pulses. Whenever the qubit is idle, it could be pulsed with small opposite pulse amplitude to slowly discharge the

capacitor and bring back the offset voltage to zero. In the context of the surface code, where the flux pulses are applied in a regular pattern, the DC bias could also be shifted such that one needs to apply a constant offset with the AWG chosen to exactly compensate the charge on the capacitor accumulated during the pulse scheme $V_{\text{comp}} = V_{\text{pulse}} T_{\text{tot}}/T_{\text{cycle}}$ where T_{tot} is the total pulse time during one cycle and T_{cycle} is the period of a error correction cycle.

3.4 Inverse Filter Calibration Procedure

In this section, I describe the procedure how the IIR and FIR filter coefficients on the warm setup are determined. I aim for a work flow, that allows to extract the filter coefficients from a single flux line measurement. Hereby, the characterization of the signal line is done with a long square pulse that approximates a step function. I use a square pulse with pulse length $T_p = 4\,\mu\text{s}$ generated on an Zurich Instruments UHF-LI (sampling rate $f_S = 1.8\,\text{GHz}$). This pulse length is chosen as trade-off between long pulse duration to capture all dynamics and short pulse length for high repetition rate to do averaging on the oscilloscope. The transient response is measured for testing purpose directly after the AWG on an LeCroy SDA 13000 oscilloscope with 10 GS/s and 1 GHz bandwidth in the 100 mV/div setting (connected to the AWG with a BNC cable), see measurement trace in Fig. 3.8 (a).

Remark regarding the scope: The oscilloscope has limited vertical accuracy (in the data sheet specified is a DC gain accuracy of $\pm 1.5\,\%$ of the full scale, no AC gain accuracy given). In general, oscilloscopes with such a wide bandwidth are typically build to be used for testing telecommunication hardware, where AC accuracy is not critical. Consequently, we do not fully trust the measurement with this device. However, we still use it to extract our predistortion filters on the warm setup, since we do not have any other device to measure such fast transient signals from DC to approximately 1 GHz. With our original goal in mind to compensate for the effects of the whole signal chain, we aim to remeasure the step response later directly on the qubits allowing for another iteration of filter extraction.

3.4.1 Iterative IIR Fitting

To find the IIR filter coefficients according to a fit of the model described in section 3.2.4 $f(t) = (A + Be^{-t/\tau})u(t)$, we start fitting this function for large $\tau \sim 1\,\mu\text{s}$ to the tail of the step response (compare figures 3.8 and 3.9). When having extracted the three IIR filter coefficients (a_1, b_0, b_1) from the fitting parameters A, B, τ, the measured data is numerically corrected by applying the corresponding inverse IIR filter to the measured data. This digital filtering modifies the time trace significantly and is justified under the assumption that the system behaves linear in good approximation.

Alternatively, the filter could be applied to the square pulse and a new measurement could be taken. However, this would be very time consuming, as the measurements are not automated so it is favorable to extract all needed filters from one physical measurement.

The fitting routine with subsequent numerical application of the inverse filter is repeated several times, each time decreasing the characteristic decay time τ of the IIR filter. The crucial point is the selection of the data range and starting values for the individual fits, such that they converge towards reasonable parameter values (see Fig. 3.8 (b) where the ranges for the first four fits are indicated). This iterative IIR filter fitting procedure returns a set of around ten IIR first-order filters. For the data set used for the example plots below, in total 13 IIR filters were

extracted. The first four fits and their corresponding fitted parameters and IIR filter coefficients are shown in Fig. 3.9, table 3.1 and 3.2, respectively. The full tables including all 13 fits are shown in appendix C.

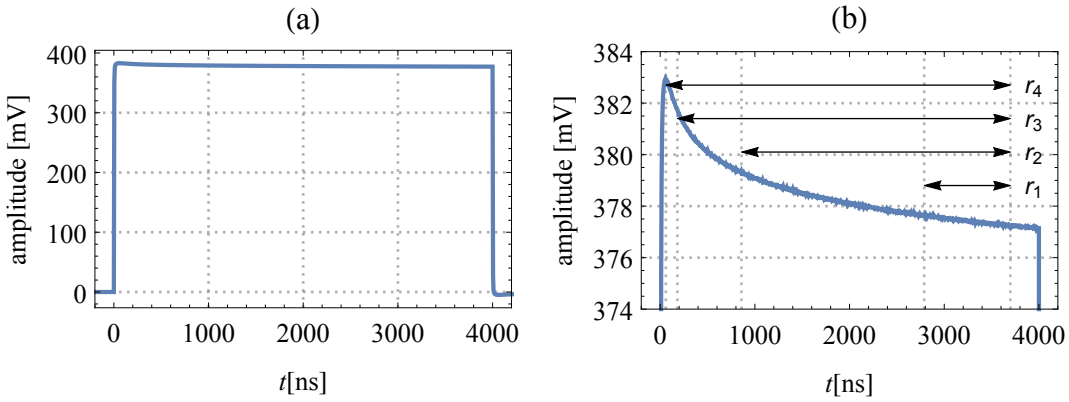

Fig. 3.8: (a) Step response: measurement of a 4 µs square pulse. (b) Zoom to the top of the pulse with indicated fitting ranges of the first four fits (compare also Fig. 3.9 fits #1 to #4).

Fit #	A[mV]	B[mV]	τ[ns]
1	375.885	−3.832 34	3557.55
2	375.880	−2.432 06	484.388
3	375.878	−2.951 19	103.034
4	375.878	3.047 91	38.756

Table 3.1: Table of the fitting parameters for first four fits with longest decay times (see also Fig. 3.9).

The very slow response corresponding to the first fit is suspected to be a feature of the oscilloscope since it depends on the settings of the scope. However, as already mentioned above, we are able to measure the step response directly on the qubits with limited temporal resolution up to approximately 10 ns. I.e., we are able to characterize especially such slow features at the cold setup including the whole signal chain what allows us to recalculate the filters (see section 4.4).

Fit #	a_1	b_0	b_1
1	0.999 845	0.994 542	−0.994 387
2	0.998 861	0.993 596	−0.992 457
3	0.994 664	0.992 231	−0.986 895
4	0.985 652	1.008 12	−0.993 768

Table 3.2: Table of the IIR first-order filter tabs extracted from the first four fits.

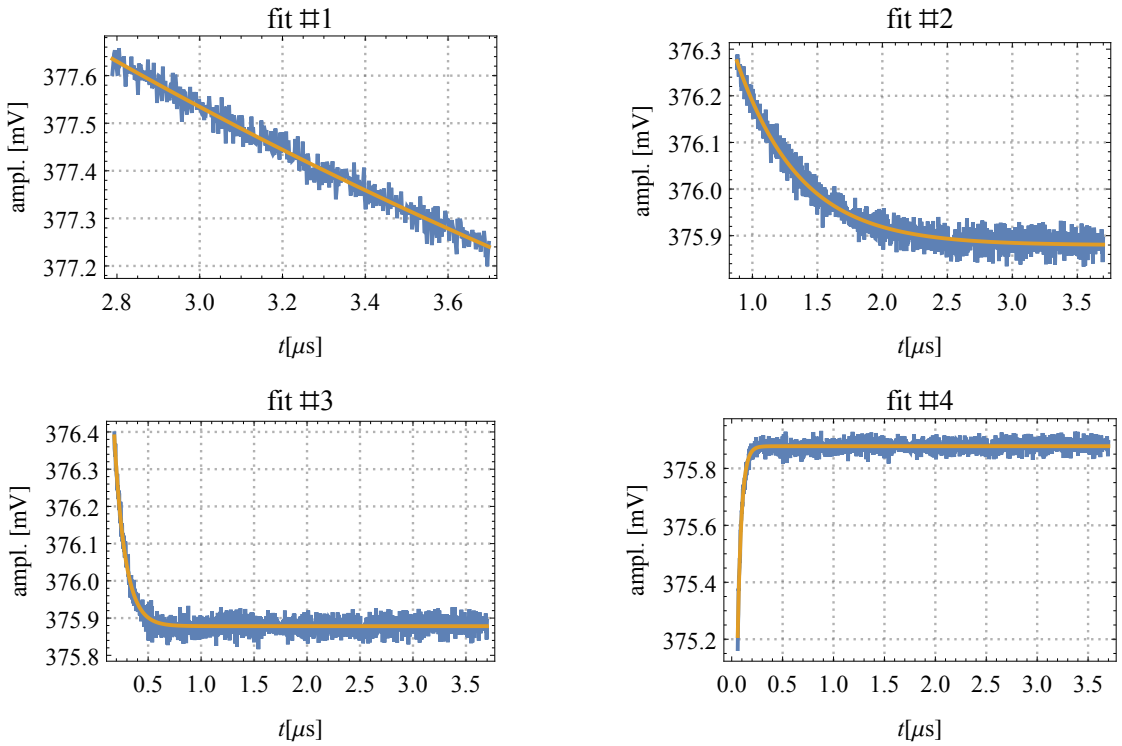

Fig. 3.9: Plots of the first four IIR fits.

3.4.2 FIR fitting

The numerically IIR corrected data is taken to calculate FIR filter coefficients to correct for imperfections on a short timescale ($\lesssim 50\,\mathrm{ns}$). Hereby, a segment of the data around the step, including fast ripples and overshoots, is taken to calculate the impulse response numerically by discrete differences (see Fig. 3.10). It is very important, that the IIR filters are sufficiently good, such that the impulse response decays back to zero very fast (inside the chosen segment) and only a small number of FIR taps is needed. From this numerically determined impulse response the FIR filter coefficients are calculated according to the procedure described in section 3.2.3. Good results are obtained for a regularization parameter $\alpha = 1.0$. Finally the leading and tailing

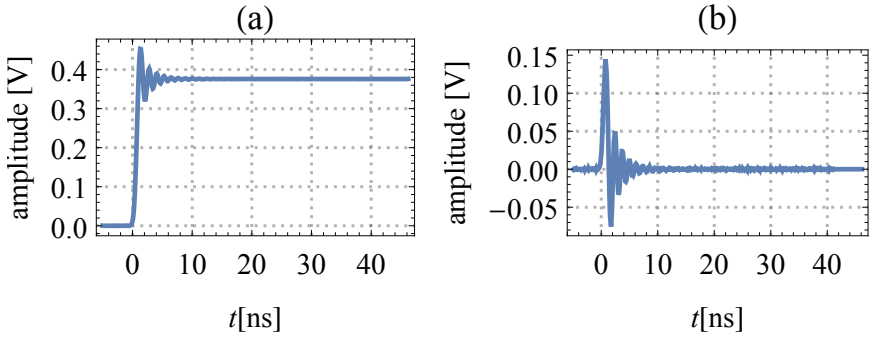

Fig. 3.10: (a) IIR corrected data taken for FIR extraction (512 data points). (b) Impulse response (of IIR corrected data) calculated by numerical differentiation of a step response (data in (a)).

zeros in the FIR filter kernel are dropped, yielding a 164-tap FIR filter in this example (see Fig. 3.11 (a)) with the power spectral density plotted in Fig. 3.11 (b). At the sampling rate of 1.8 GS/s this FIR filter length corresponds to 91 ns. Due to the regularization the FIR filter kernel is low-pass filtered. I want to emphasize, that it is essential to get good IIR filters first and correct the data to get an FIR filter with a reasonable number of FIR tabs.

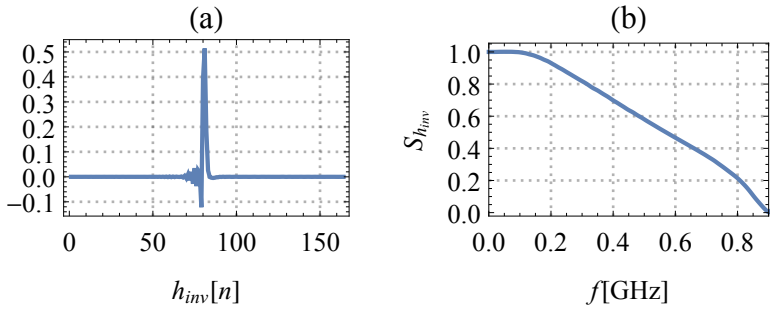

Fig. 3.11: (a) FIR filter coefficients for regularization parameter $\alpha = 1$. (b) Power spectral density of the FIR filter coefficients.

Results for different regularization parameters α are plotted in the appendix (see Fig. C.4). These plots also visualize the low-pass filtering effect of the total variation regularization depending on α. After having applied all the corrections, a predistorted pulse was remeasured. For optimal results one more IIR fit was performed (see Fig. 3.12) and added to the list of IIR filters, yielding a total of 14 IIR filters.

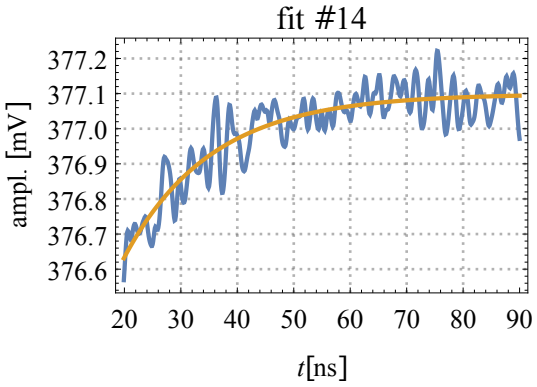

Fig. 3.12: Additional 14th IIR fit for optimal pulse shape ($\tau = 15.44$ ns, filter coefficients $a_1 = 0.964\,508$, $b_0 = 1.004\,44$ and $b_1 = -0.968\,951$).

3.5 Pulse Shaping

Having extracted all the IIR filters and the FIR filter kernel, an arbitrary pulse can be predistorted with these linear filters. Up to now, this is done offline on a computer. See Fig. 3.13 for the example of shaping an 50 ns Gaussian smoothed square pulse.

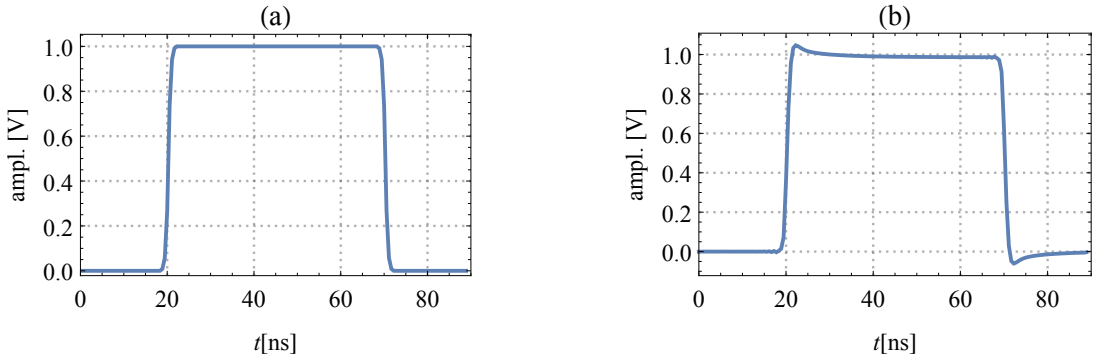

Fig. 3.13: (a) Intended pulse shape (50 ns square pulse smoothed with a $\sigma = 1$ ns Gaussian filter kernel) with rise time $t_r \approx 2.6$ ns (10-to-90 rise time). (b) Pulse pattern predistorted with inverse IIR and FIR filters.

3.5.1 Demo Results

To test the performance of the predistortion filters, we compiled a square pulse pattern with 50 ns pulse width filtered with a Gaussian filter kernel of width $\sigma = 1$ ns corresponding to a 10-to-90 rise time $t_r = 2.56$ ns (see also Fig. 3.13). For this pulse, measurements were done with and without predistortion filters and plotted in Fig. 3.14 together with the intended Gaussian smoothed square pulse in orange (pulse profile fitted). The shaped pulse reproduces a Gaussian smoothed pulse much better. Outside the region around the rising and falling edge (ca. 5 ns window), the maximal deviation is below 0.5 mV which is roughly 0.1 % of the pulse height. The relative large deviation at the pulse edges comes due to non-Gaussian filtering effects of the FIR predistortion filter, that changes the shape of rising and falling edge slightly. In contrary to the unshaped pulse, the shaped one does not suffer of over- and undershoots, nor of wiggles on top of the pulse (see Fig. 3.14 (b)).

It is tempting to reduce the regularization parameter α for better correction of fast oscillations and reduced non-Gaussian filtering due to the finite bandwidth of the FIR filter. However, this increases the amplitude of fast oscillations in the FIR filter which can not be reproduced well on the AWG and could possibly lead to non-linear behavior. I.e., to our knowledge, we reached the boarder of what is possible to correct with the limited bandwidth and resolution of the AWG.

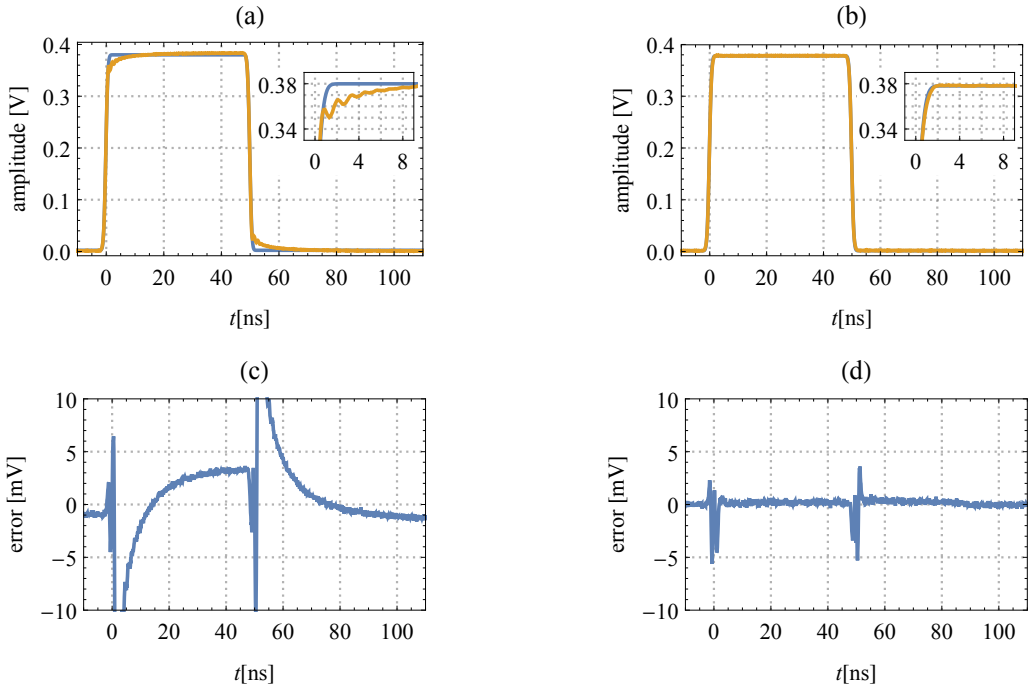

Fig. 3.14: Comparison of unshaped and shaped pulse. Upper plots: (a) Measurement of an unshaped 50 ns square pulse (1 ns Gaussian filtered) in orange; intended Gaussian smoothed square pulse in blue (parameters fitted). (b) Measurement of the same pulse with prior applied predistortion filters (shaped pulse); measured data (orange) and Gaussian smoothed square pulse (parameters fitted) in blue overlay almost perfectly. The insets are zooms to the top of the pulse edge. Lower plots (c) and (d): corresponding deviation of the measured pulse shape (orange line in upper plot) from the optimal pulse shape (blue line in upper plot). The predistorted pulse approximates the intended pulse shape much better as seen in (d).

3.6 Conclusions

In this chapter, we developed a procedure to extract both inverse FIR and IIR filters from a step response measurement. The regularization scheme used to invert the FIR filter proves to be robust against noise on the measured data and improves previously used methods [Bozyigit2010b, Baur2012b, Johnson2011PhD]. The IIR filters, well suited to be applied in real time on an AWG successfully correct distortions on a slow timescale. We demonstrated that we can produce very flat square pulses (within 0.1 % of the pulse amplitude after less than 5 ns) using our predistortion filters. Additionally, we showed how to calculate an IIR filter, that corrects for the distortions caused by a bias-T and cleared the way to use it in our setup to suppress $1/f$ noise increasing the coherence times of the qubits.

Chapter 4

Experimental Part

After having prepared theoretical background and developed a procedure to efficiently calculate inverse filters, in this chapter, we finally get our hands on the experiment working towards a high-fidelity two-qubit gate.

4.1 Measurement Setup

Our current sample M85BM2 consists of eight qubits arranged in a linear chain, meaning that the connectivity of the eight qubits is a 1D chain with coupling resonators between nearest neighbors (brown lines in Fig. 4.2). The designed maximum frequencies are chosen, such that all the qubits can be parked with 400 MHz distance to their neighbors (see qubit parking scheme in Fig. 4.1). Our samples are fabricated on 500 µm thick sapphire wafers coated with a 150 nm Niobium film on top. In a first step the resonator, gate line and flux line structures are written onto the chip in a photolithograpic process. Then, in a second step, the Josephson junctions are fabricated out of aluminum and aluminum oxide by electron-beam lithography. The qubits are designed with a cross-shaped charge island, also called Xmon [Barends2013], which allows for coupling to two bus resonators in addition to the readout resonator and the drive line (see also Fig. 4.2). Our experiments are conducted at the base temperature of a BlueFors dilution refrigerator at 12 mK. This has mainly two reasons. In the first place, only below 1.2 K aluminum gets superconductively and, secondly, the thermal energy needs to be much lower than the energy scale

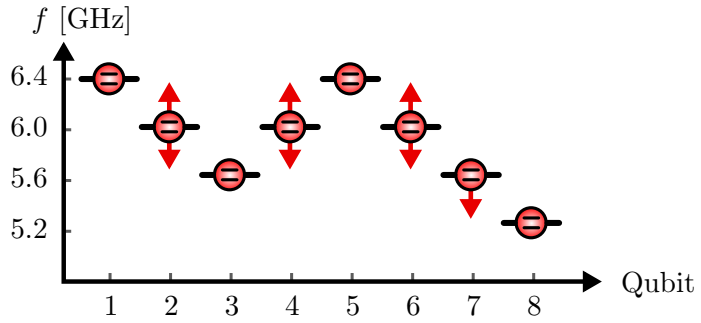

Fig. 4.1: Scheme of the parking frequencies planned for the 8-qubit sample. The red arrows indicate the qubits to be used for the C-Phase gates. Qubits 3, 7 and 8 are designed to have maximum frequency 5.6 GHz, all others 6.4 GHz.

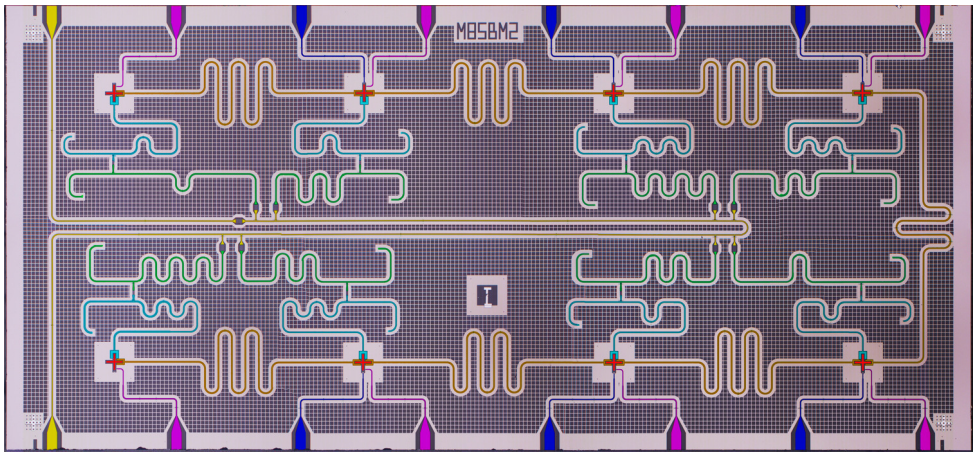

Fig. 4.2: False color micrograph of our eight qubit sample M85BM2. The eight Xmon qubits are colored in red. In yellow is the readout line, with all eight qubits coupled to (via readout resonators in blue and and Purcell filter in green). Neighboring qubits are coupled through a bus resonator (brown), each qubit has an individual drive line (purple) and qubits 2 to 7 have a flux line (blue).

we use for our qubits to reduce thermal excitation to a minimum amount. Further, the qubits decay always to their ground state due to energy relaxation and are thus passively initialized in the $|0\rangle$ state.

Each qubit has two control lines: the drive line and the flux line (see Fig. 4.3). Each drive line is controlled by two AWG channels sending the two quadratures for single qubit pulses, that are upconverted to the RF frequency in an IQ mixer. The RF frequencies are delivered by microwave generators (Rohde & Schwarz SGS100A). All the drive lines are attenuated and thermalized by three 20dB attenuators at the 4K, the 100mK and the 12mK stages of the refrigerator to reduce thermal noise.
The currents through the flux lines are driven by Stanford Research Systems (SRS) SIM928 DC voltage sources, that are galvanically isolated and have low noise. The flux line of qubit 6 used to drive the two-qubit gates is connected to an Tektronix AWG5014c via a bias-T (Mini Circuits ZFBT-4R2GW+) and an additional 20dB attenuator (see Fig. 4.3). Inside the fridge, the flux lines are attenuated with a 20dB attenuator thermalized at the 4K plate to reduce thermal noise and filtered with a Mini Circuits VLFX780 low-pass filter at base temperature. The home made Eccosorb filter is used to block infrared photons that pass the low-pass filter.
The readout line is based on a homodyne detection scheme. The complex quadratures of the readout pulses are generated on a Zurich Instruments UHFQC and upconverted with an IQ mixer. The signal then passes the readout line on the sample and is amplified with a broad-band, near-quantum noise limited traveling-wave parametric amplifier [Macklin2015] at base temperature, a high electron mobility transistor (HEMT) amplifier at 4K and room temperature amplifiers. It gets down-converted with an IQ mixer and then digitized on the same UHFQC as used for the pulse generation. This device can do real time data processing, as digital down-conversion, integrated readout and averaging (see also [Remm2017] for a detailed description of the readout scheme). All the instruments are controlled by the Python based open-source software PycQED initiated by QuTech, Delft University of Technology which is built on top of the QCoDeS data acquisition framework.

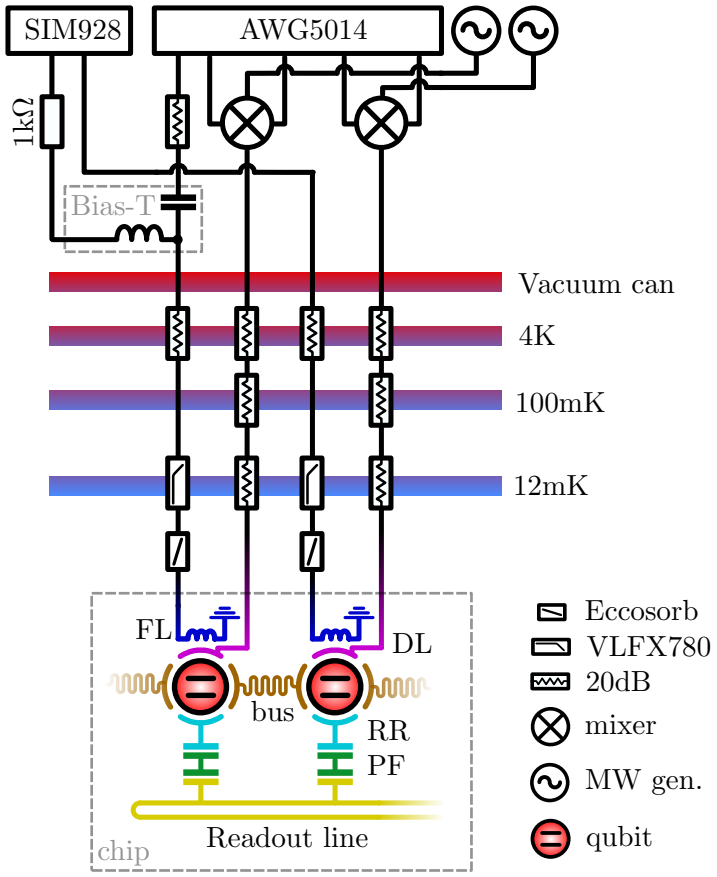

Fig. 4.3: Schematic of the experimental setup with room temperature electronics used to control the qubits, fridge wiring and sample. Flux lines (FL) and drive lines (DL) used to drive gates on Qb6 (left) and Qb7 (right). The colors correspond to the ones used in Fig. 4.2. RR: readout resonator, PF: Purcell filter.

4.1.1 Inverse Filter Calibration on the Warm Setup

The step response of the warm flux lines for two qubits (Qb4 and Qb6) was measured when the cryostat was opened to mount the sample (no bias-T's installed yet). The signal was generated on the same AWG channel later used for the experiments and the response was measured with our LeCroy SDA13000 oscilloscope connected the the SMP connector where the sample holder will be plugged in. On both data sets the IIR and FIR fitting routines were run to extract the inverse filters (for flux line FL6 fits see Appendix C). Additionally, the functionality to use these filters for offline predistortion (also the IIR filters planned to run on the AWG in the future) was implemented in PycQED.

4.2 Sample Characterization

To tune up the full functionality of the quantum processor and for a future iteration of design improvement, all sample parameters such as readout frequency, maximum qubit frequency, dispersive shift, flux offset and coherence times need to be characterized. Automated routines for single qubit gate calibration were developed in [Balasiu2017]. Here, I focus on the characterization of the bus resonators.

4.2.1 Parking Qubits

The qubit pair best suited to test two-qubit gates on the sample M85BM2 are qubits Qb6 and Qb7 with maximum frequencies $f^6_{\max} = 5.92\,\text{GHz}$ and $f^7_{\max} = 5.44\,\text{GHz}$. The optimal flux bias points were chosen manually, such that the qubits were parked at their maximum frequency with $\Delta = f^6_{\max} - f^7_{\max} = 480\,\text{MHz}$. Having both qubits parked at their sweet spot is preferable for high coherence times T_2 ($T_2^6 \sim 8\,\mu\text{s}$ and $T_2^7 \sim 5\,\mu\text{s}$ at their maximum frequency). The qubit anharmonicities $\alpha^6 = 234\,\text{MHz}$ and $\alpha^7 = 238\,\text{MHz}$ are measured with high-power spectroscopy on the $|0\rangle \rightarrow |2\rangle$ two photon transition.

4.2.2 Bus Resonator Spectroscopy

The bus resonator frequencies were measured spectroscopically by driving the drive lines with high power. Due to small but finite capacitive coupling between drive line and bus resonator the latter can be populated with a high power drive. Photons in the bus resonator induce an AC Stark shift of the qubit frequency, which is measured as a slight change in the frequency of the readout resonator (compare section 2.1.2). Due to the small coupling, the peak appears only at very high drive power (see Fig. 4.4(a)). Since the experiment is equivalent to qubit spectroscopy, the existing fitting routine to extract the qubit frequency can be used (see Fig. 4.4(b)). All measured bus resonator frequencies are listed in table 4.1. The bus frequencies are chosen in an alternating pattern, i.e., matching pairs between neighbors can be identified as the common bus resonator. For qubits Qb6 and Qb7 the matching frequency is $f^{6,7}_{\text{bus}} = 7.850\,\text{GHz}$.

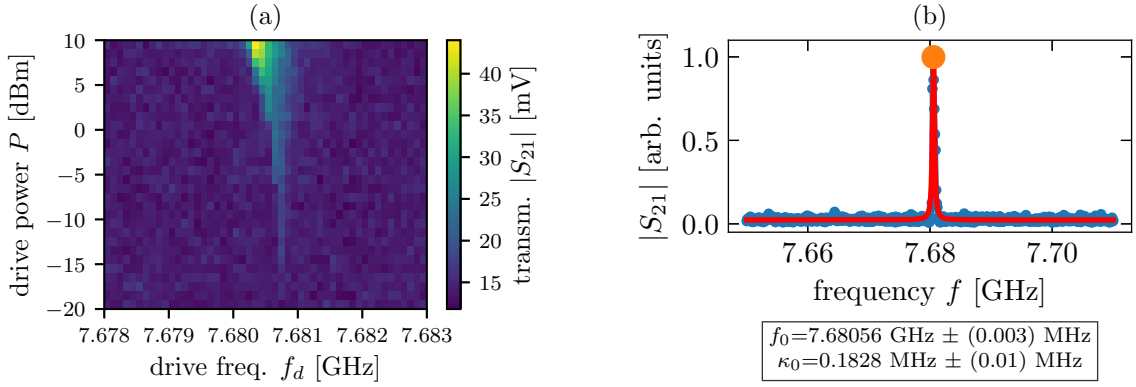

Fig. 4.4: (a) Qubit spectroscopy on Qb6 at one of the bus resonator frequencies for different drive power. Only for very high power the resonator appears. (b) Automated qubit spectroscopy fit used to fit the bus resonator (drive power $P = 0\,\text{dBm}$).

Qubit #	f_q[GHz]	bus 1 [GHz]	bus 2 [GHz]
2	6.255	7.687	7.859
3	5.216	7.687	7.860
5	6.451	7.680	7.849
6	5.917	7.680	7.850
7	5.441	7.670	7.850

Table 4.1: Table of the qubit frequencies f_q and the bus resonator frequencies measured on each qubit.

4.2.3 Spectroscopic J-Coupling Measurement

In order to measure the coupling strength between two qubits, we performed spectroscopy on the avoided crossing. While sweeping the flux bias, pulsed spectroscopy was measured on one of the qubits. I.e., while sweeping the drive frequency on the qubit drive line, the transmission of the readout line was measured at the frequency of corresponding readout resonator. Unlike for continuous tone spectroscopy, in pulsed spectroscopy the drive tone is turned off during the readout [Balasiu2017] with the advantage, that no AC shift is present due to photons in the readout resonator.
The flux bias range was chosen, such that the frequency of one of the qubits was tuned through the parking frequency of its neighboring qubit, i.e., through the avoided-crossing. In this range, the flux dependency of the qubit transition frequencies can be linearly approximated with $\omega_i(\Phi)/2\pi = f_i(\Phi) \sim f_{i,0}(1 + c_i(V_{\text{bias}} - V_{\text{bias},0})$. The energy levels through the anti-crossing are given by the eigenvalues of the simplified Hamiltonian

$$\widehat{H} = \hbar \begin{pmatrix} \omega_i(\Phi) & J \\ J & \omega_{i+1}(\Phi) \end{pmatrix}. \tag{4.1}$$

To extract the bus mediated coupling J, these eigenvalues are fitted to the peaks of the measured transmission spectra (see Fig. 4.5 solid lines). Using equation 2.7 the coupling between qubit and

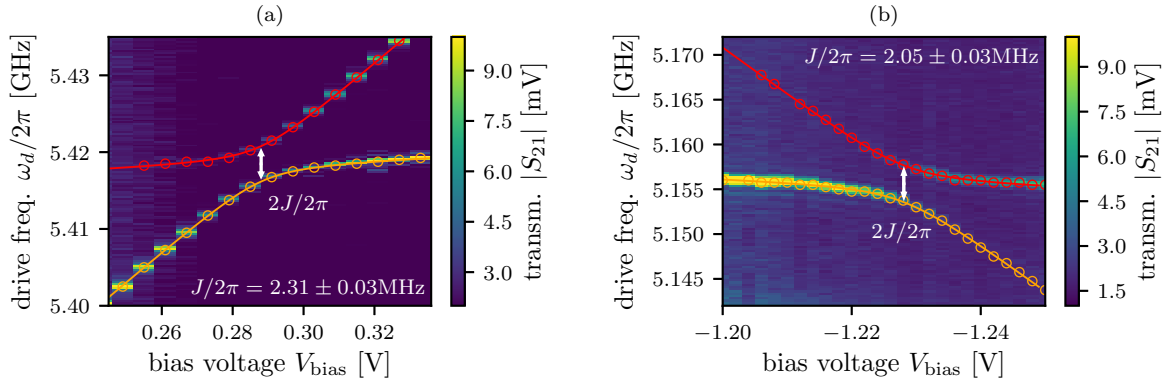

Fig. 4.5: Pulsed spectroscopy of the avoided crossing between quits Qb6 & Qb7 in (a) and between qubits Qb2 & Qb3 in (b). The red and orange circles are the peaks assigned to upper and lower branch, respectively. The solid lines are fits according to the model 4.1. The fitted bus mediated coupling rates are $J_{6,7}/2\pi = 2.31(3)$ MHz and $J_{2,3}/2\pi = 2.05(3)$ MHz. In (a) Qb6 was tuned to cross Qb7, while spectroscopy on Qb6 was performed. (b) shows combined data from spectroscopic measurements on both Qb2 and Qb3 while tuning the frequency of Qb2.

bus resonator can be estimated at the interaction point under the approximation $g = g_6 \sim g_7$ (symmetric design):

$$g/2\pi = \sqrt{\Delta J}/2\pi \sim 75\,\mathrm{MHz} \tag{4.2}$$

evaluated for qubits Qb6 and Qb7. The smaller coupling between qubits Qb2 and Qb3 can be explained by the larger detuning from the bus resonator. However, for both pairs the measured values for J is approximately 20 % lower than designed due to too small coupling g_i. This gives us already a lower bound for the C-Phase gate time $t_g = 2\pi/(2\sqrt{2}J) \sim 153\,\mathrm{ns}$.

4.2.4 Flux Pulses: Connecting the AWG

As a next step towards performing two qubit gates, a channel of the Tektronix AWG5014 was connected to the flux line. As discussed in section 2.2, the coherence times depend strongly on the flux noise. I.e., the room temperature cabling has to be chosen in a clever way, not to worsen the dephasing time of the qubit significantly by the additional electronic $1/f$ noise from the AWG. We tested the influence of the additional electronic noise on the coherence times of the qubit in different configurations.
Typically, we operate our qubits at sweet spot, where they are first-order insensitive to flux noise (compare Eq. 2.9). However, for the characterization of the coherence times we want to be susceptible to noise. Thus, to determine the flux noise dependence on the cabling configuration, all measurements were performed at sweet spot and also approximately 200 MHz below sweet spot. Regarding two qubit gates, it is also important to have an estimate of the dephasing during the flux pulse when the qubit leaves its sweet spot.
For the characterization of the phase stability, T_2^* and T_1 were measured as e.g. described in Ref. [Baur2012b]. T_2^* is the decay time of a Ramsey signal and gives a lower bound for T_2. All coherence times measured in different cabling configurations are listed in table 4.2. Either the coil, mounted below the chip or the flux line is used to set the flux bias.
Summarizing these results, we can conclude, that the naive way of connecting the AWG to the flux line making use of the 'add input' option for the DC bias decreases T_2^* by approximately factor 10. I.e., according to formula 2.9 the $1/f$ noise amplitude is approximately 10 times higher compared to the situation when biasing directly with the SRS DC source. This is in good accordance with the measured noise spectra of the DC voltage source and the AWG channel (see Fig. A.2 and A.4 in the appendix).
Connecting an additional 20dB attenuator and biasing through a bias-T turn out to be the optimal solution to suppress low frequency noise from the AWG, such that the dephasing time is not critically affected (cabling in Fig. 4.3). In this configuration the measured T_2^* was only lowered by a factor of 0.7 , hence an increase of the electronic noise amplitude of approximately factor 1.4. To compensate for the bias-T an additional IIR filter, that was determined in an offline measurement of the bias-T was added to the IIR filter list (fit in Fig. B.1 (b) in the appendix).

Flux line config.	parking	f_q [GHz]	T_2^* [μs]	T_1 [μs]	V_{coil} [mV]	V_{FL6} [mV]
All shorted	SS	5.927	8.8(4)	6.7	-140	shorted
All shorted	200BS	5.725	2.62(6)	7.1	132	shorted
FL6 connected to SRS (no voltage divider)	SS	5.927	8.3(3)	6.6	-140	0
FL6 connected to SRS (no voltage divider)	200BS	5.724	2.46(10)	6.0	132	0
FL6 connected to AWG	SS	5.927	5.59(27)	6.9	-140	0
FL6 connected to AWG	200BS	5.744	0.319(12)	6.9	132	0
FL6 connected to AWG, biased with FL6	SS	5.927	8.7(3)	7.0	shorted	780
FL6 connected to AWG, biased with FL6	200BS	5.739	0.310(13)	7.0	shorted	-870
FL6 connected to AWG, biased with FL6, 0.1V ampl.	SS	5.927	7.77(23)	7.0	shorted	780
FL6 connected to AWG, biased with FL6, 0.1V ampl.	200BS	5.728	0.64(3)	6.3	shorted	-870
All FL's connected, biased with FL6 through AWG	SS	5.927	9.3(4)	6.7	shorted	780
All FL's connected, biased with FL6 through AWG	200BS	5.739	0.300(17)	6.7	shorted	-870
All FL's connected, FL6 bias through AWG, 20dB attenuation	200BS	5.721	1.52(4)	5.9	shorted	-8700
All FL's connected, FL6 bias with bias-T	200BS	5.719	0.412(5)	6.9	shorted	-770
All FL's connected, FL6 bias with bias-T, 20dB attenuation	200BS	5.741	1.754(22)	7.5	shorted	-7700

Table 4.2: Dephasing times measured in different flux line configurations. Legend: SS: sweet spot; 200BS: qubit parked 200 MHz below sweet spot; 0.1V ampl.: AWG output range set to 0.1 V_{pp}; f_q: qubit frequency; V_{coil}: coil voltage; V_{FL6}: flux line 6 voltage

4.3 Flux Pulse Calibration

Having the AWG connected to the flux line, we are now able to apply flux pulses to the qubit. In semi-rigid cables with teflon as dielectric material, the signal speed is approximately 20 cm/ns. Thus, for optimal timing of the flux pulses relative to drive and readout pulses, we need to calibrate the timing of the flux pulse channel to compensate for differences in cable length. Further we want to relate the pulse amplitude to the induced flux and frequency offset.

4.3.1 Timing

To measure the relative timing of flux pulses and drive pulses (e.g. a $\pi/2$-pulse), a Ramsey like phase measurement was programmed. A $(\pi/2)_X$-pulse brings the qubit into a superposition of ground and excited state $|\psi\rangle = (|0\rangle + |1\rangle)/\sqrt{2}$, and the second $\pi/2$-pulse, delayed by 200 ns brings the qubit to its final state that is read out (RO pulse, compare also Fig. 4.6 (a) for the pulse scheme). Sweeping the phase θ of the second $\pi/2$-pulse results in a final qubit state with oscillating excited state population $P_{|1\rangle} = \cos(\theta)$. Interleaving the two pulses with a short 20 ns flux pulse, introduces a phase shift $\theta \to \theta + \phi$ as long as the flux pulse is in between the two $\pi/2$-pulses. This phase shift ϕ can be fitted. The calibration measurement is therefore performed as a 2D sweep, where in one dimension the phase θ of the second $\pi/2$-pulse and in the second dimension the relative delay of the flux pulse is swept. It is important to sweep the delay in multiples of the AWG sampling period to omit quantization artifacts.
As long as the flux pulse is outside of the 200 ns window framed by the two $\pi/2$-pulses, no phase shift is expected ($\phi = 0$). All fitted phase shifts (black dots in Fig. 4.6) are once more fitted with a smooth window function (sum of two erf functions) to extract the time of rising and falling edges, which give information about the timing relative to the drive pulses. This calibration measurement and its analysis were implemented in PycQED in a method of the qubit

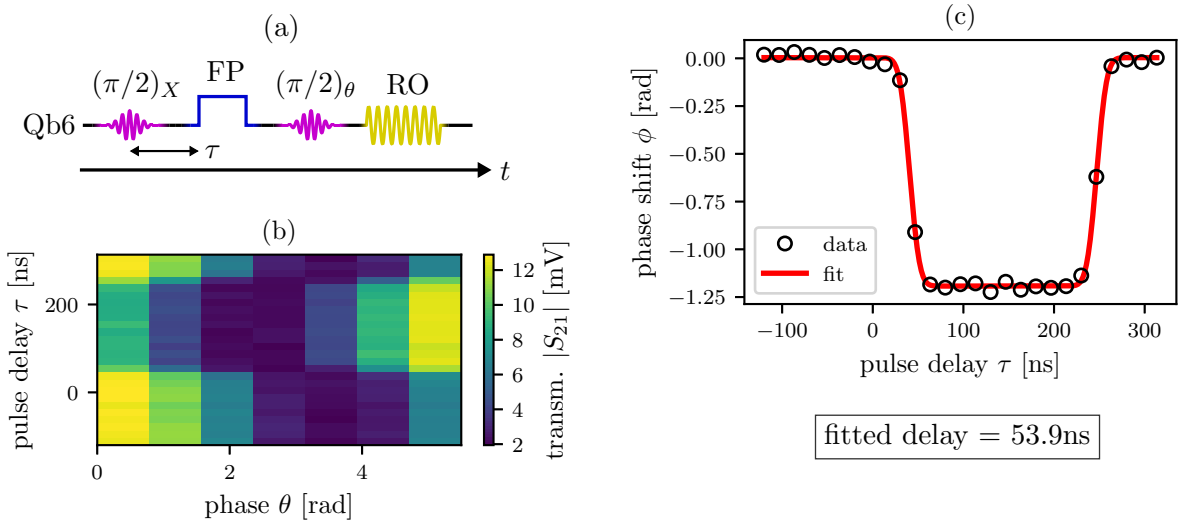

Fig. 4.6: Timing calibration: (a) pulse scheme of the two dimensional calibration measurement (phase θ and delay τ are being swept; Qb6: qubit 6, FP: flux pulse, RO: readout pulse). (b) Raw measurement data. In (c) the fitted phase shifts ϕ are plotted (black dots) and in red is the fitted error function model to extract the relative pulse delay of 53.9 ns

object (`calibrate_flux_pulse_timing`) such that the determined channel delay is automatically updated and compensated in future experiments.

4.3.2 Amplitude

For the calibration of the flux pulse amplitude, a very similar measurement was conducted where instead of the flux pulse delay its amplitude was swept (see also pulse scheme in Fig. 4.7 (a)). The timing was chosen, such that the flux pulse with length $T_p = 50\,\text{ns}$ was in between the two $\pi/2$-pulses. The phase shift ϕ can directly be related to the qubit frequency shift $\Delta f = \phi/(2\pi T_p)$ (see Fig. 4.7 (b)). On the other hand, the flux pulse amplitude A is related to the magnetic flux $\Phi/\Phi_0 = A/c$, where the parameter c quantifies the volt per flux quantum periodicity. Substituting the magnetic flux in the qubit frequency Eq. 2.1 with A allows to fit this equation when sweeping the flux pulse amplitude A and determine the volt per flux quantity $c = 0.512(16)\,\text{V}/\Phi_0$ (not using an additional 20dB attenuator at room temperature; including this additional attenuation increases the ratio by a factor of 10, i.e., $c_{20\text{dB}} = 5.12\,\text{V}/\Phi_0$). This calibration is very important, since it gives the relation between flux pulse amplitude A and qubit frequency $f_q = f_q^{\max} - \Delta f(A)$ and will be used to predict the pulse amplitude for the C-Phase gate.

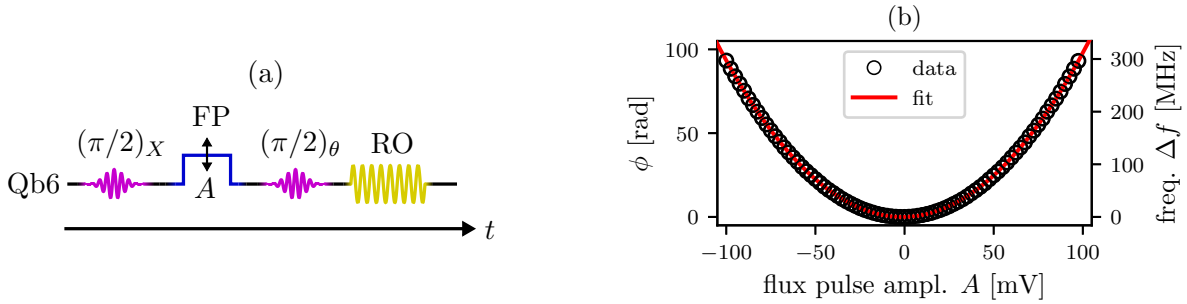

Fig. 4.7: Frequency calibration. (a) shows the pulse scheme analogous to Fig. 4.6 (a), but sweeping the flux pulse amplitude A (Qb6: qubit 6, FP: flux pulse, RO: readout pulse). (b) Fitted phase shifts (black dots) and fit of Eq. 2.1 to extract the volt per flux quantum periodicity $c = 0.512(16)\,\text{V}/\Phi_0$.

4.4 Flux Pulse Scope

Ideally, we want to measure the step response in terms of qubit frequency, such that all the characteristics of the cold signal chain including SMP connectors to the sample and inductive coupling to the SQUID loop are determined. A very precise measurement of the qubit frequency can be done in a Ramsey type measurement analogous to section 4.3.2. However, the temporal resolution is limited by the length of the two $\pi/2$-pulses and the period in between, where the phase of the qubit evolves dependent on the qubit frequency. Another approach with much higher resolution in the time domain is the π-pulse based scope mode, where the frequency of a π-pulse is swept [Johnson2011PhD, Baur2012b]. Alternative schemes are described in [Ciorciaro2017] and [Jerger2017]. However, both of them are also limited in temporal resolution.

4.4.1 The π-Pulse Scope

When sweeping the drive frequency of a π-pulse with a Gaussian spectral profile, the measured excited state population along the drive frequency axis fits very well to a Gaussian function. This is not clear a priori, because off-resonant driving could change the line shape. However, as we expect the line to be symmetric, it is sufficient to extract the center of the line with any fit to monitor the qubit frequency at a specific time τ. Now when sweeping also the delay τ relative to the flux pulse, as depicted in Fig. 4.8 (a), a two dimensional image of the flux pulse is generated (see Fig. 4.8 (b)). To extract an approximate form of the pulse shape, each frequency slice is fitted with a Gaussian model to extract the peak frequency. The fitted qubit frequency, respectively its detuning with respect to the parking frequency can then be converted to a flux pulse voltage using the frequency calibration from section 4.3.2. For comparison, the same experiment was also done, without using any inverse filters (see Fig. 4.9 (a)). Then the distortion caused by the bias-T visually dominates the behavior for large τ.

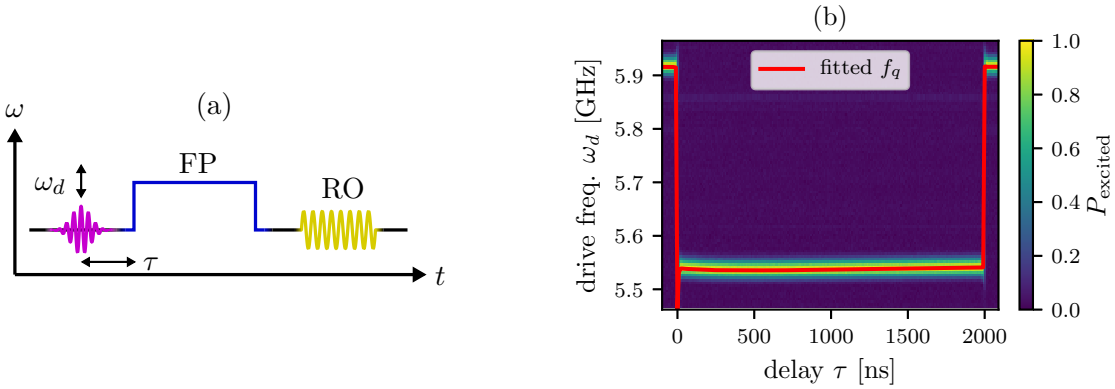

Fig. 4.8: Flux pulse scope: (a) pulse scheme of the scope mode: drive frequency ω_d and delay τ relative to the flux pulse of a π-pulse are swept. In (b) the excited state population of the qubit Qb6 is shown with the fitted qubit frequency (red line).

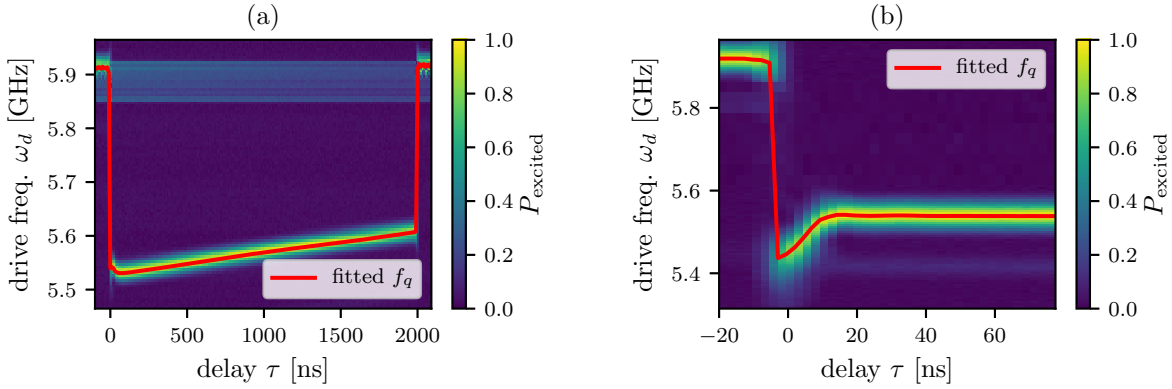

Fig. 4.9: Flux pulse scope. (a) Flux scope measurement and fitted frequencies (red line) without any filters applied. The visually dominating distortion comes from the bias-T. (b) Zoom in the the edge in Fig. 4.8 (b).

A zoom into the edge of the square pulse shows the limits of this method (Fig. 4.9 (b)). For optimal resolution, the π-pulse was chosen as short as possible (Gaussian pulse width $\sigma = 5\,\text{ns}$). However, it still introduces e temporal blur of approximately 10 ns, that prevents fitting an FIR filter and hence doing the full characterization of the transfer function with the described method on the cold setup.

4.4.2 IIR Filters Revisited

With this new information on the response of the signal chain, we can further improve our set of filters by fitting additional IIR filters to the data in Fig. 4.8 (b) and Fig. 4.9 (b) (fits in Fig. 4.10 (a) and (b), respectively). With six additional IIR filters, we were able to reduce the overshoot at the step significantly and flatten the top of a 2 µs pulse to a total drift below 0.2 % of the pulse height with space for even further improvement down to the resolution of the AWG (see Fig. 4.11).

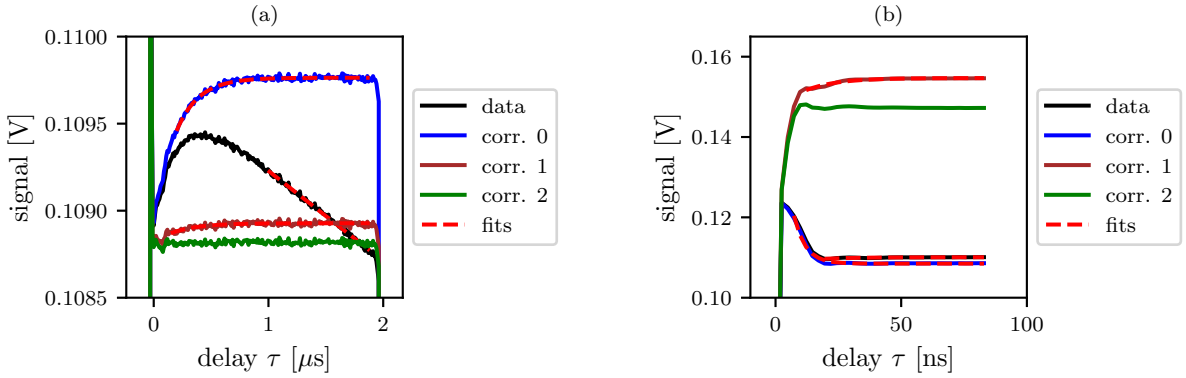

Fig. 4.10: Additional IIR fits done with the data measured in the flux scope mode analogous to the IIR fitting procedure in section 3.4.1. (a) Data taken from flux scope measurement in Fig. 4.8 (b). (b) Data taken from 4.9 (b).

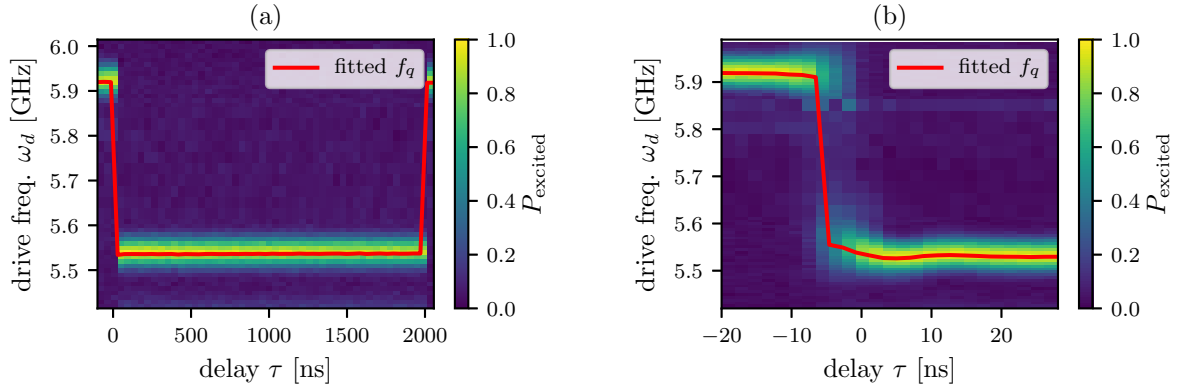

Fig. 4.11: Flux pulse scope image of a pulse using the additional IIR filters from Fig. 4.10. The top of the pulse is very flat (a) while the overshoot is significantly reduced (b).

4.5 C-Phase Gate Calibration

In the non-adiabatic case, we only need to optimize two parameters, the pulse amplitude A and the pulse length T_p. To do so, we must be able to measure some objective function, i.e., a quantity that characterizes the quality of our C-Phase gate. In a first step, the population retrieved in the $|11\rangle$ state is measured in form of a Chevron pattern.

4.5.1 Retrieved Population: Chevron Pattern

The Chevron pattern arises when two interacting levels coherently exchange population. In our case, when we start in the $|11\rangle$ state, its population oscillates between the $|11\rangle$ and the $|20\rangle$ state when being on resonance. The oscillation frequency between these two levels is $\Omega/2\pi = \sqrt{(2\sqrt{2}J)^2 + \Delta^2}/2\pi$ [Steffen2013a], i.e., it increases with the detuning Δ between the two interacting levels. Thus, the Chevron pattern allows us to measure J and the retrieved $|11\rangle$ state population after an arbitrary interaction time T_p. The pulse sequence is illustrated in Fig. 4.12 (a). The system is initialized in the $|11\rangle$ state with a π-pulse on each qubit. The flux pulse brings the $|11\rangle$ level close to resonance with the $|20\rangle$ level and lets them interact for time T_p. Then the state of qubit Qb7 is read out. Its excited state population $P_{|1\rangle}$ represents the population of the $|11\rangle$ state. By fitting, an exponential decaying cosine to the horizontal slices of Chevron pattern, the coupling energy $J = 2.362(8)\,\mathrm{MHz}$ was determined in good accordance with the spectroscopically measured value. This confirms also, that the C-Phase gate will take approximately 150 ns. At this flux pulse amplitude $A = 0.7725\,\mathrm{V}$ with $\Delta = 0$ the signal decays on a time scale $\tau = 1.7(2)\,\mu\mathrm{s}$, giving an upper bound to the fidelity of the C-Phase gate due to finite dephasing time T_2.

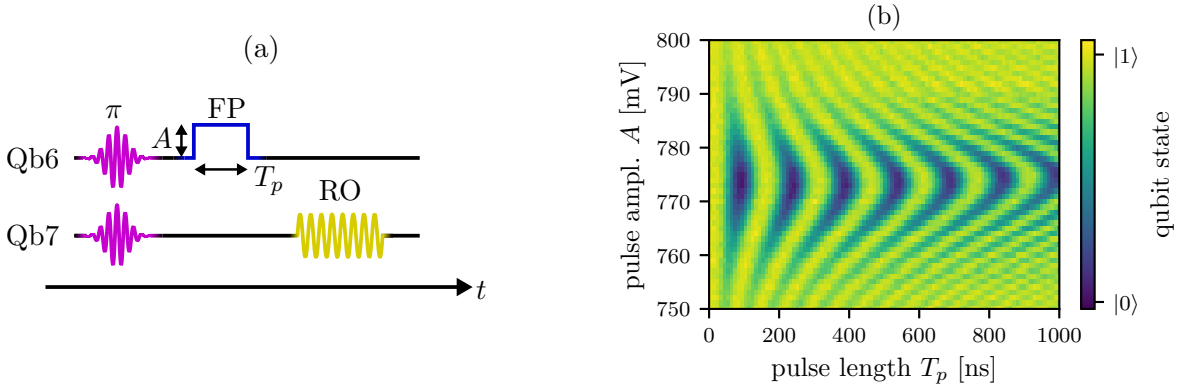

Fig. 4.12: Chevron Pattern. (a) Pulse scheme of the Chevron pattern measurement, the π-pulses initialize the system in the $|11\rangle$ state and the flux pulse with amplitude A turns the interaction on for the time T_p; qubit Qb7 is read out (RO: readout pulse). (b) 2D plot of the measured qubit population on qubit 7. The qubit state is calibrated using dedicated calibration points (not shown in the plot).

4.5.2 Conditional Phase Measurement

For the full characterization of the C-Phase gate, we also need to measure the conditionally acquired phase. This can be done in a very similar measurement, where the system is prepared in a superposition state $(|10\rangle + |11\rangle)/\sqrt{2}$. Dependent on the conditional phase acquired on the $|11\rangle$ state, a final $(\pi/2)_\theta$-pulse on qubit 7 brings the qubit into a phase dependent superposition of $|0\rangle$ and $|1\rangle$. Sweeping the phase of the second $\pi/2$ pulse, allows to fit a cosine model and extract the phase. This is essentially the same as interleaving a Ramsey type phase measurement with the conditional phase gate. The fitted phase still includes the single qubit dynamic phases. Hence, in a reference experiment without preparing qubit 6 in the excited state, the pure dynamical phase is measured. Subtracting this dynamical from the fitted phase yields the conditional phase. This time-consuming 3D measurement mainly serves to give an idea how the phase landscape looks like. For the optimization of the flux pulse parameters with a convenient algorithm, only a few points in this landscape actually have to be measured. However, from this plot it can be inferred, that the conditional phase close optimal pulse length $T_p \sim 150\,\text{ns}$ is first order insensitive to the pulse length. This decouples the conditional phase in some sense from the retrieved amplitude, which is first order insensitive to the flux pulse amplitude at that parameter spot allowing for orthogonal optimization of both parameters.

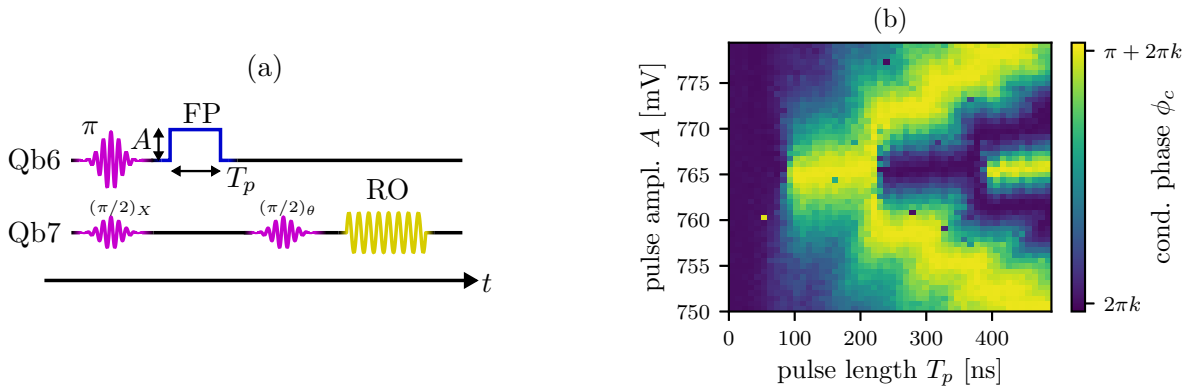

Fig. 4.13: Conditional phase measurement. (a) Pulse scheme: Qb7 is prepared in a superposition state, whereas Qb6 is either prepared in the excited or in the ground state for the reference measurements. For the full measurement, flux pulse amplitude A, length T_p and the angle of the second $\pi/2$-pulse on Qb7 are swept. (b) Calculated relative phase in dependence of flux pulse amplitude and length plotted with a periodic color map. Note the center amplitude $A = 765\,\text{mV}$ differs from previous measurements, due to slight changes in the parking positions.

4.5.3 Gate Calibration: Nelder Mead Optimization

Finally, we can stick the population and the phase measurement together and run an optimization algorithm. The retrieved population can even be extracted as the amplitude of the oscillations in the phase fits, speeding up the algorithm. The cost function, also called objective function, is programmed, such that it is minimal for maximum retrieved population and conditional phase being exactly $\phi_c = \pi + 2\pi k$ for some k. For the optimization, the Nelder-Mead algorithm [Nelder1965], a so-called downhill simplex method, is well suited since it is very robust against noise.
For the qubit pair Qb6 and Qb7, the optimal flux pulse parameters $A = 765.0\,\text{mA}$ and $T_p = 148\,\text{ns}$

were found (see Fig. 4.14), which is very close to the spectroscopically predicted value. However, the phase measurements are very sensitive to qubit frequency drifts, since Qb6 is far away from sweet spot and hence susceptible to magnetic flux noise during the C-Phase gate. Hence, for feasibility it crucial to have very stable qubits with drifts $\Delta f \ll J$ on the timescale of calibration and measurements.

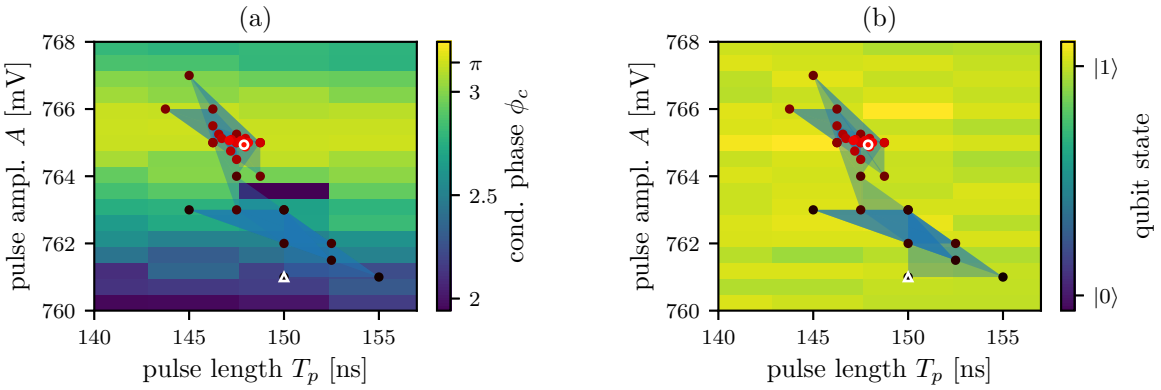

Fig. 4.14: Illustration of the Nelder-Mead algorithm optimizing the phase (a) and the amplitude (b) shown in the background. The white triangle depicts the initial point from where the algorithm starts to converge toward the optimal value (white circle: $A = 765.0\,\mathrm{mA}$ and $T_p = 148\,\mathrm{ns}$). The order of the measured points in the parameter parameter space is indicated with the transition from black to red. The light blue simplices are used to estimate the gradient.

Chapter 5

Conclusions and Outlook

In this thesis, we developed different tools to characterize the flux line and extract filters for flux pulses, such as the flux pulse scope, the regularized FIR fitting procedure and the fitting and the inversion of the exponential IIR model. These tools were used in a procedure to calibrate IIR and FIR predistortion filters for scalable fast two-qubit flux gates. The IIR filters are planned to be implemented in real time on the ZI HDAWG, however, this is yet under development.
To apply flux pulses to a qubit, we connected an AWG channel to the corresponding flux line using a bias-T to set the DC bias and filter out $1/f$ noise from the AWG. The noise from the AWG and its effect on the coherence times was characterized. We found that T_2^* is only affected slightly by the additional noise from the AWG channel (0.7 times shorter than without the AWG connected when being measured 200 MHz below sweet spot). The pulse distortions caused by the bias-T were successfully removed with an inverse IIR filter.
Working towards the tune-up and optimization of a C-Phase gate, we measured the Chevron pattern and the conditional phase after a flux pulse and ran the Nelder-Mead optimization algorithm to optimize the pulse parameters. To complete the C-Phase gate, the dynamic phase of the individual qubits still have to be corrected using zero-time virtual Z-gates. Further optimization and characterization of the gate with Bell state tomography, process tomography and interleaved randomized benchmarking are currently in preparation. Fast fidelity measurements allow even further optimization of a few parameters describing the analytic pulse shape, e.g. the 'fast-adiabatic pulse' [Martinis2014a]. If the gate performance can be measured fast enough also the short time response (FIR filter) could be optimized pixel wise, e.g., with an evolutionary algorithm.
In regard of future applications, a automated tune-up still has to be programmed in a way that is feasible for large scale quantum processors. At the same time, all IIR filters should be measured with the flux pulse scope and applied as real time filters on the Zurich Instruments HDAWG. Furthermore, for high-fidelity gates it is crucial to improve the qubit stability. Also when reducing the gate time by larger coupling rage J, the on-off ratio gets critical requiring a non-trivial identity gate. This problem could potentially be solved with tunable resonators, that can be tuned far off-resonant between two gates.

Acknowledgment

I want to thank Dr. Sebastian Krinner for supervising my Master's Thesis in a way, that I could work very independent and felt appreciated as a scientist and also as a person. Professor Andreas Wallraff I want to thank for leading the QuDev Lab, such that we could do research at the forefront of the field of experimental quantum computing and giving useful input in our weekly team meetings. Further I want to thank Johannes Heinsoo, Christian Kraglund Andersen and Christopher Eichler for their experimental and theoretical expertise on many occasions. Stefania Balasiu, Ants Remm and Simon Storz I thank for their support, the close collaboration and the friendly atmosphere. I want to thank Paul Magnard for many interesting scientific lessons and Janis Lütolf for technical support. Finally, I also thank all other members of the QuDev for all the help that I can not mention here.

Bibliography

[Balasiu2017] Stefania Balasiu. Single-qubit gates calibration in pycqed using superconducting qubits. Master's thesis, ETH Zurich, 2017.

[Barends2013] R. Barends, J. Kelly, A. Megrant, D. Sank, E. Jeffrey, Y. Chen, Y. Yin, B. Chiaro, J. Mutus, C. Neill, P. O'Malley, P. Roushan, J. Wenner, T. C. White, A. N. Cleland, and John M. Martinis. Coherent josephson qubit suitable for scalable quantum integrated circuits. *Phys. Rev. Lett.*, 111(8):080502–, August 2013.

[Barends2014] R. Barends, J. Kelly, A. Megrant, A. Veitia, D. Sank, E. Jeffrey, T. C. White, J. Mutus, A. G. Fowler, B. Campbell, Y. Chen, Z. Chen, B. Chiaro, A. Dunsworth, C. Neill, P. O/'Malley, P. Roushan, A. Vainsencher, J. Wenner, A. N. Korotkov, A. N. Cleland, and John M. Martinis. Superconducting quantum circuits at the surface code threshold for fault tolerance. *Nature*, 508(7497):500–503, Apr 2014. Letter.

[Baur2012b] Matthias Baur. *Realizing quantum gates and algorithms with three superconducting qubits*. PhD thesis, ETH Zurich, 03 2012.

[Bell1980] D A Bell. A survey of 1/f noise in electrical conductors. *Journal of Physics C: Solid State Physics*, 13(24):4425, 1980.

[Blais2004] Alexandre Blais, Ren-Shou Huang, Andreas Wallraff, S. M. Girvin, and R. J. Schoelkopf. Cavity quantum electrodynamics for superconducting electrical circuits: An architecture for quantum computation. *Phys. Rev. A*, 69:062320, Jun 2004.

[Blais2007] A. Blais, J. Gambetta, A. Wallraff, D. I. Schuster, S. M. Girvin, M. H. Devoret, and R. J. Schoelkopf. Quantum-information processing with circuit quantum electrodynamics. *Phys. Rev. A*, 75(3):032329–21, March 2007.

[Bombin2013] H. Bombin. An introduction to topological quantum codes. *"Topological Codes", in "Quantum Error Correction", edited by Daniel A. Lidar and Todd A. Brun, Cambridge University Press, New York,*, 2013, November 2013.

[Bozyigit2010b] Deniz Bozyigit. Correlation function measurements of a microwave frequency single photon source. Master's thesis, ETH Zurich, 04 2010.

[Chow2011] Jerry M. Chow, A. D. Córcoles, Jay M. Gambetta, Chad Rigetti, B. R. Johnson, John A. Smolin, J. R. Rozen, George A. Keefe, Mary B. Rothwell, Mark B. Ketchen, and M. Steffen. Simple all-microwave entangling gate for fixed-frequency superconducting qubits. *Phys. Rev. Lett.*, 107:080502, Aug 2011.

[Ciorciaro2017] L. Ciorciaro. Calibration of flux line distortions for two-qubit gates in superconducting qubits, 10 2017.

[Cirac1995] J. I. Cirac and P. Zoller. Quantum computations with cold trapped ions. *Phys. Rev. Lett.*, 74:4091–4094, May 1995.

[Clarke2008] John Clarke and Frank K. Wilhelm. Superconducting quantum bits. *Nature*, 453(7198):1031–1042, June 2008.

[Devoret1997] M. H. Devoret. Quantum fluctuations in electrical circuits. In S. Reynaud, E. Giacobino, and J. Zinn-Justin, editors, *Quantum Fluctuations: Les Houches Session LXIII*, pages 351–386. Elsevier, 1997.

[Devoret2004] M. H. Devoret, A. Wallraff, and J. M. Martinis. Superconducting qubits: A short review. *arXiv:cond-mat/0411174*, 2004.

[Dhawan1985] Atam Prakash Dhawan, Rangaraj M. Rangayyan, and Richard Gordon. Image restoration by wiener deconvolution in limited-view computed tomography. *Appl. Opt.*, 24(23):4013–4020, Dec 1985.

[DiCarlo2009] L. DiCarlo, J. M. Chow, J. M. Gambetta, Lev S. Bishop, B. R. Johnson, D. I. Schuster, J. Majer, A. Blais, L. Frunzio, S. M. Girvin, and R. J. Schoelkopf. Demonstration of two-qubit algorithms with a superconducting quantum processor. *Nature*, 460(7252):240–244, July 2009.

[DiCarlo2010] L. DiCarlo, M. D. Reed, L. Sun, B. R. Johnson, J. M. Chow, J. M. Gambetta, L. Frunzio, S. M. Girvin, M. H. Devoret, and R. J. Schoelkopf. Preparation and measurement of three-qubit entanglement in a superconducting circuit. *Nature*, 467:574–578, 2010.

[Dutt2007] M. V. Gurudev Dutt, L. Childress, L. Jiang, E. Togan, J. Maze, F. Jelezko, A. S. Zibrov, P. R. Hemmer, and M. D. Lukin. Quantum register based on individual electronic and nuclear spin qubits in diamond. *Science*, 316(5829):1312–1316, 2007.

[Feynman1982] Richard P. Feynman. Simulating physics with computers. *Int. J. Theor. Phys.*, 21(6):467–488, June 1982.

[Fowler2012] Austin G. Fowler, Matteo Mariantoni, John M. Martinis, and Andrew N. Cleland. Surface codes: Towards practical large-scale quantum computation. *Phys. Rev. A*, 86:032324, Sep 2012.

[Ghosh2013] Joydip Ghosh, Andrei Galiautdinov, Zhongyuan Zhou, Alexander N. Korotkov, John M. Martinis, and Michael R. Geller. High-fidelity controlled-σ^Z gate for resonator-based superconducting quantum computers. *Phys. Rev. A*, 87:022309, Feb 2013.

[Havelock2008] D. Havelock, S. Kuwano, and M. Vorländer. *Handbook of Signal Processing in Acoustics*. Springer New York, 2008.

[Horsman2012] Clare Horsman, Austin G Fowler, Simon Devitt, and Rodney Van Meter. Surface code quantum computing by lattice surgery. *New Journal of Physics*, 14(12):123011, 2012.

[Jerger2017] Markus Jerger, ZÃ©non Vasseli, and Arkady Fedorov. In situ characterization of qubit control lines: a qubit as a vector network analyzer, 2017.

[Johnson1928] J. B. Johnson. Thermal agitation of electricity in conductors. *Phys. Rev.*, 32:97–109, Jul 1928.

[Johnson2011PhD] Blake Johnson. *Controlling Photons in Superconducting Electrical Circuits*. PhD thesis, Yale, 2011.

[Katsaggelos2012] Aggelos K. Katsaggelos. *Digital Image Restoration*. Springer Publishing Company, Incorporated, 2012.

[Kelly2014] J. Kelly, R. Barends, B. Campbell, Y. Chen, Z. Chen, B. Chiaro, A. Dunsworth, A. G. Fowler, I. C. Hoi, E. Jeffrey, A. Megrant, J. Mutus, C. Neill, P. J. J. O'Malley, C. Quintana, P. Roushan, D. Sank, A. Vainsencher, J. Wenner, T. C. White, A. N. Cleland, and John M. Martinis. Optimal quantum control using randomized benchmarking. *Phys. Rev. Lett.*, 112,:240504, March 2014.

[Kitaev1996] A Kitaev. Quantum measurements and the abelian stabilizer problem. eccc tr96-003. *arXiv preprint quant-ph/9511026*, 23, 1996.

[Koch2007] Jens Koch, Terri M. Yu, Jay Gambetta, A. A. Houck, D. I. Schuster, J. Majer, Alexandre Blais, M. H. Devoret, S. M. Girvin, and R. J. Schoelkopf. Charge-insensitive qubit design derived from the Cooper pair box. *Phys. Rev. A*, 76(4):042319, 2007.

[Laplante1999] Phillip A. Laplante. *Comprehensive Dictionary of Electrical Engineering (Electrical Engineering Handbook)*. Springer, 1999.

[Leek2009] P. J. Leek, S. Filipp, P. Maurer, M. Baur, R. Bianchetti, J. M. Fink, M. Göppl, L. Steffen, and A. Wallraff. Using sideband transitions for two-qubit operations in superconducting circuits. *Phys. Rev. B*, 79:180511, 2009.

[Lucy1974] L. B. Lucy. An iterative technique for the rectification of observed distributions. *The Astrophysical Journal*, 79:745, June 1974.

[Lyons1996] Richard G. Lyons. *Understanding Digital Signal Processing*. Addison-Wesley Longman Publishing Co., Inc., Boston, MA, USA, 1st edition, 1996.

[Macklin2015] C. Macklin, K. O'Brien, D. Hover, M. E. Schwartz, V. Bolkhovsky, X. Zhang, W. D. Oliver, and I. Siddiqi. A near-quantum-limited josephson traveling-wave parametric amplifier. *Science*, 350(6258):307–310, 2015.

[Majer2007] J. Majer, J. M. Chow, J. M. Gambetta, J. Koch, B. R. Johnson, J. A. Schreier, L. Frunzio, D. I. Schuster, A. A. Houck, A. Wallraff, A. Blais, M. H. Devoret, S. M. Girvin, and R. J. Schoelkopf. Coupling superconducting qubits via a cavity bus. *Nature*, 449(7161):443–447, September 2007.

[Martinis2014a] John M. Martinis and Michael R. Geller. Fast adiabatic qubit gates using only σ_z control. *Phys. Rev. A*, 90:022307, Aug 2014.

[McKay2017] David C. McKay, Christopher J. Wood, Sarah Sheldon, Jerry M. Chow, and Jay M. Gambetta. Efficient z gates for quantum computing. *Phys. Rev. A*, 96:022330, Aug 2017.

[Moore1965] Moore. Cramming more components onto integrated circuits. *Electronics*, 38(8), April 1965.

[Nelder1965] J. A. Nelder and R. Mead. A simplex method for function minimization. *The Computer Journal*, 7(4):308–313, 1965.

[Nielsen2000] Michael A. Nielsen and Isaac L. Chuang. *Quantum Computation and Quantum Information*. Cambridge University Press, 2000.

[OMalley2016] Peter O'Malley. *Superconducting Qubits: Dephasing and Quantum Chemistry*. PhD thesis, UC Santa Barbara, 06 2016.

[Preskill2012] John Preskill. Quantum computing and the entanglement frontier. In *25th Solvay Conference on Physics, October 19-22, 2011, Brussels, Belgium.*, 2012.

[Raussendorf2007] Robert Raussendorf and Jim Harrington. Fault-tolerant quantum computation with high threshold in two dimensions. *Phys. Rev. Lett.*, 98:190504, May 2007.

[Remm2017] Ants Remm. Implementation and characterization of multiplexed readout of superconducting qubits. Master's thesis, ETH Zurich, 2017.

[Richardson1972] William Hadley Richardson. Bayesian-based iterative method of image restoration∗. *J. Opt. Soc. Am.*, 62(1):55–59, Jan 1972.

[Rudin1992] Leonid I. Rudin, Stanley Osher, and Emad Fatemi. Nonlinear total variation based noise removal algorithms. *Physica D: Nonlinear Phenomena*, 60(1):259 – 268, 1992.

[Sheldon2016] Sarah Sheldon, Easwar Magesan, Jerry M. Chow, and Jay M. Gambetta. Procedure for systematically tuning up cross-talk in the cross-resonance gate. *Phys. Rev. A*, 93:060302, Jun 2016.

[Shor1994] P. W. Shor. Algorithms for quantum computation: Discrete logarithms and factoring. In *Proceedings, 35th Annual Symposium on Foundations of Computer Science, Santa Fe*, page 124. IEEE Computer Society Press, 1994.

[Shor1995] Peter W. Shor. Scheme for reducing decoherence in quantum computer memory. *Phys. Rev. A*, 52:R2493–R2496, Oct 1995.

[Smith1997] Steven W. Smith. *The Scientist and Engineer's Guide to Digital Signal Processing*. California Technical Publishing, San Diego, CA, USA, 1997.

[Stan2002] Guy-Bart Stan, Jean-Jacques Embrechts, and Dominique Archambeau. Comparison of different impulse response measurement techniques. *J. Audio Eng. Soc*, 50(4):249–262, 2002.

[Steffen2013a] Lars Steffen. *Quantum Teleportation and Efficient Process Verification with Superconducting Circuits*. PhD thesis, ETH Zurich, 2013.

[Strauch2003] Frederick W. Strauch, Philip R. Johnson, Alex J. Dragt, C. J. Lobb, J. R. Anderson, and F. C. Wellstood. Quantum logic gates for coupled superconducting phase qubits. *Phys. Rev. Lett.*, 91(16):167005, October 2003.

[Terhal2013] B. M. Terhal. Quantum error correction for quantum memories. *ArXiv e-prints*, page 2013arXiv1302.3428T, February 2013.

[Tikhonov1963] A. N. Tikhonov. Solution of incorrectly formulated problems and the regularization method. *Soviet Math. Dokl.*, 4:1035–1038, 1963.

[Versluis2017] R. Versluis, S. Poletto, N. Khammassi, B. Tarasinski, N. Haider, D. J. Michalak, A. Bruno, K. Bertels, and L. DiCarlo. Scalable quantum circuit and control for a superconducting surface code. *Phys. Rev. Applied*, 8:034021, Sep 2017.

[Wallraff2007] A. Wallraff, D. I. Schuster, A. Blais, J. M. Gambetta, J. Schreier, L. Frunzio, M. H. Devoret, S. M. Girvin, and R. J. Schoelkopf. Sideband transitions and two-tone spectroscopy of a superconducting qubit strongly coupled to an on-chip cavity. *Phys. Rev. Lett.*, 99:050501, 2007.

[Yurke1984] Bernard Yurke and John S. Denker. Quantum network theory. *Phys. Rev. A*, 29(3):1419–1437, Mar 1984.

Appendix A

Noise

As mentioned in section 2.2, different sources of noise can significantly influence the dephasing times of the qubits. Here, a short introduction to noise sources is given and a method to measure the output noise of electronic devices is presented.

A.1 Thermal Noise and Electronic $1/f$ Noise

Thermal noise, also Johnson-Nyquist noise [Johnson1928], is electronic noise generated by thermal charge fluctuations with a flat spectrum. This type of frequency independent noise is also called white noise. In contrast, noise with a power spectral density $P(f) \propto 1/f$ is called $1/f$ or pink noise [Bell1980]. Typically electronic devices as AWGs suffer from such $1/f$ noise [OMalley2016] (see also Fig. A.2 AWG5014 $4\,\mathrm{V_{pp}}$ measurement). To achieve lowest possible noise on our qubits for optimal coherence times and gate fidelities, ideally the AWG output is high-pass filtered in a manner, that the $1/f$ noise is pushed below the thermal noise floor (flat spectrum above 1 MHz in Fig. A.3).

A.2 Noise Measurements on a ZI HF2LI

The Zurich Instruments HF2LI lock-in amplifier is an all-digital device, that operates at a maximal sampling rate of 210 MSa/s and has an analog bandwidth of 50 MHz with a 14 bit resolution. Internally, it uses digital oscillators with freely selectable frequencies up to 50 MHz to down-convert the digitized input signals. It is specified to have very low internal noise (below $5\,\mathrm{nV}/\sqrt{\mathrm{Hz}}$ above 1 kHz) making it well suited for noise characterization of electronic devices.
Noise spectra can be measured on the HF2LI with three different modes: Scope mode (FFT), Spectrum Analyzer mode and Sweeper mode. With appropriate settings, the noise spectra measured in these different modes coincide (see Fig. A.1). However, the Sweeper mode is most suited for simple noise characterization measurements, since the Scope and the Spectrum Analyzer mode have a number of disadvantages (limited resolution for low frequencies, only linear sweep points, residual effects of the internal filters, etc.).
In the *Sweeper* noise measurement, the digitized input signal is down-converted with the oscillator frequency f_{osc}, essentially shifting the noise at f_{osc} to 0 Hz. Then, a digital low-pass filter is applied and the root mean square voltage V_{RMS} of the signal amplitude is calculated. Finally, the noise power spectral density $\mathrm{PSD} = V_{\mathrm{RMS}}/\sqrt{B_{\mathrm{NEPBW}}}$ is determined from the RMS voltage

by dividing through the square root of the noise equivalent power bandwidth B_{NEPBW} of the low-pass filter. The HF2LI software allows to chose logarithmically spaced frequency points and automatically adapted bandwidth of the low-pass filter to speed up the measurement. Furthermore, it is very important to note, that the input coupling mode has significant effect on the measurement. In the AC coupling setting, the input signal is filtered by a capacitive high-pass filter with a cut-off frequency of 1 kHz. I.e., all measurements below 1 kHz must be measured in the DC mode while noise measurements above 1 kHz should be measured in the AC coupling mode for minimal self-noise of the device (compare Fig. A.1 (b)). Here, all plotted noise spectra are combined datasets, that are measured in DC mode below 1 kHz and in AC mode above 1 kHz. The reference traces (self-noise of the HF2LI) are measured on a terminated input (50 Ω termination).

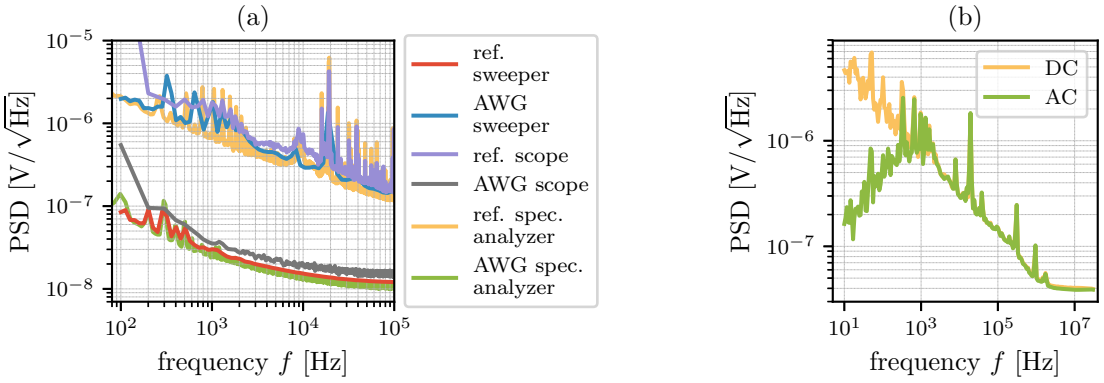

Fig. A.1: (a) Comparison of the HF2LI noise measurement modes: Scope, Spectrum Analyzer and Sweeper mode. In all modes the noise of an Tektronix AWG5014 and for comparison the noise of a 50 Ω terminated input channel (self noise) was measured. (b) Comparison of the AWG5014 in AC and DC modes. In the AC mode, the noise below 1 kHz is attenuated by the high-pass filter, in return, the HF2LI has lower self noise for frequencies above 1 kHz.

A.2.1 AWG Noise Measurements

Here, noise measurements of the Tektronix AWG5014 and the Zurich Instruments UHFAWG in different output modes are presented. They are performed in the Sweeper mode with the same settings for all measurements (see Fig. A.3). From the measured data, it can be concluded, that the UHFAWG performs very similar to the AWG5014 in direct mode (no output amplifier after the DAC). However, the output amplifier of the AWG5014 adds a significant amount of noise.

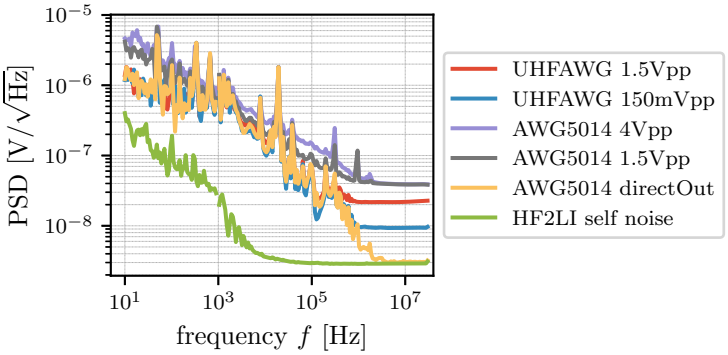

Fig. A.2: AWG noise spectra of a Tektronix AWG5014 and a ZI UHFAWG in different output settings measured on the HF2LI.

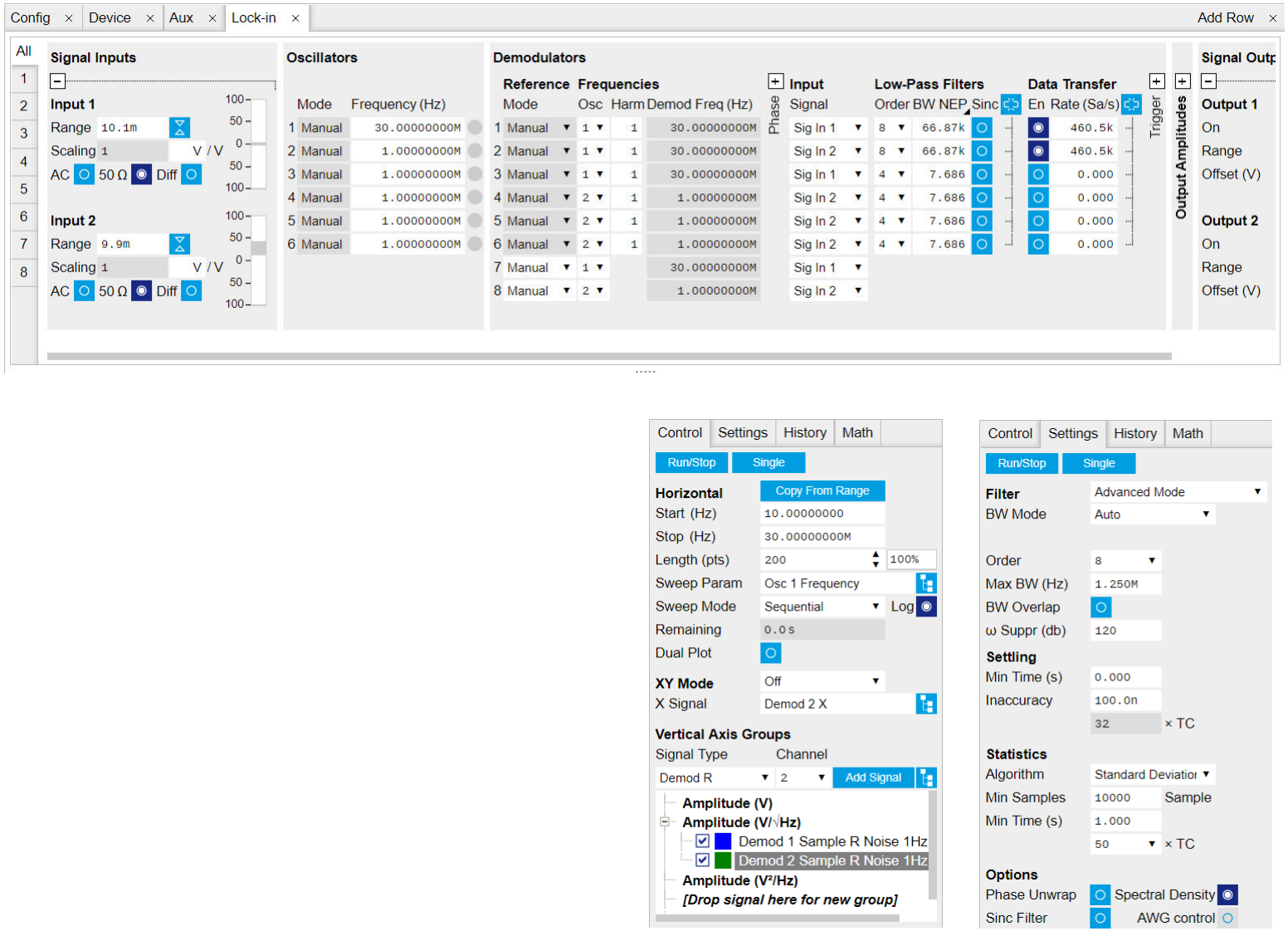

Fig. A.3: Screen shots of all settings in the HF2LI sweeper mode used in the noise measurements (DC coupling used below 1 kHz and AC coupling above).

A.2.2 SRS SIM928 DC Source Noise Measurement

We also measured the noise performance of our SRS SIM928 DC voltage sources used to drive the bias currents through the flux lines. Interestingly, they have unexpected high-frequency noise above 1 MHz. This shows the importance of proper low-pass filtering of the flux lines. For comparison, the measurement was repeated with an Mini Circuits BLP-1.9+ low-pass filter connected. A small fraction of the noise feature still makes it through the filter, i.e., for optimal usage a filter with even lower cut-off frequency is necessary.

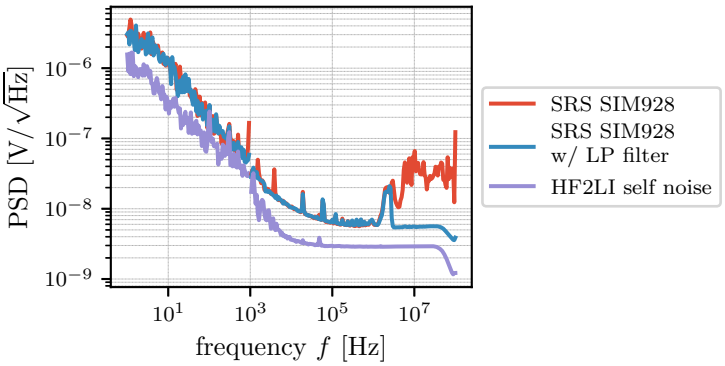

Fig. A.4: Output noise characterization of an SRS SIM928 voltage source. The device has unexpected high-frequency noise above 1 MHz, that can be filtered out by with a low-pass filter.

Appendix B

Bias-T

In our setup, we want to make use of a bias-T to reduce low-frequency noise on the flux line coming from the AWG while still being able to apply a DC bias as described in section 3.3. To choose a suitable bias-T, the step response of different bias-Ts were measured. Further, we show that the high-pass filter approximation used in section 3.3.1 is justified for the specific bias-T model we use and discuss the usage of an additional resistor to discharge the bias-T over time in the context of section 3.3.2.

B.1 Bias-T Step Responses

To verify our simplified model, we measured the step response of three different bias-T models (Mini Circuits ZFBT-4R2GW+, the Mini Circuits ZX85-12G+ and Anritsu K251; see B.1 (a)). Indeed, the only one that shows an non-oscillating exponential decay is the ZFBT-4R2GW+. This is also the bias-T model we installed in our setup since it satisfies the simplified high-pass model. The wiggles seen in the step response of the other bias-Ts can be understood as oscillations of an LC oscillator formed by the inductance and the capacitance in the bias-T. This is also verified in a simulation showing the same oscillations when including the inductance and the internal resistance of the DC source in the model. Depending on the system parameters, the

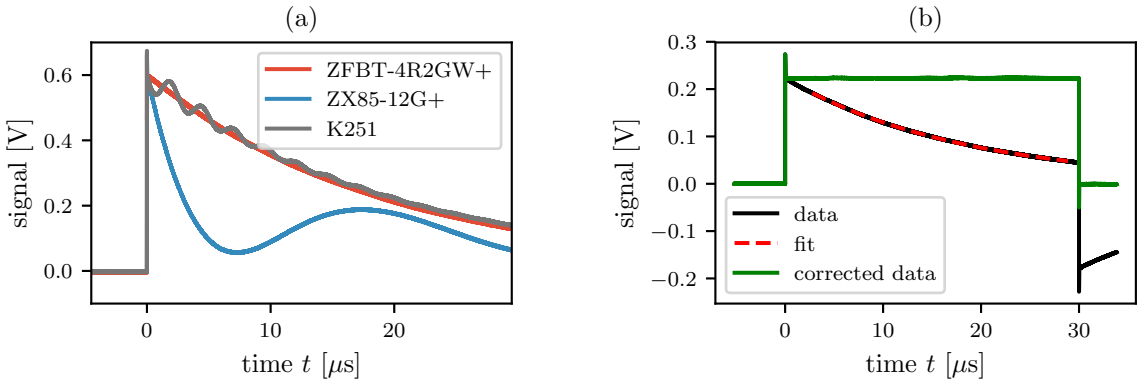

Fig. B.1: (a) Bias-T step responses for three different models. Depending on the internal capacitance and inductance, the bias-T shows oscillations (K251) or an exponential decay (ZFBT-4R2GW+). The measurements were taken with open DC port. (b) Step response of the ZFBT-4R2GW+ bias-T (black line) with exponential IIR model fit (red dashed line) and numerically inverse filtered data (green line).

oscillations are either well visible (K251) or overdamped (ZFBT-4R2GW+). The step response of the ZFBT-4R2GW+ bias-T is used to fit the IIR filter model described in section 3.3.1 and extract the predistortion filter coefficients (see B.1 (b)).

B.2 Discharge Resistor

As a possible solution for the out-of-range issue, we simulated the system with a parallel resistor added to the capacitor in the bias-T (circuit model in Fig. B.2). Applying the predistortion filter

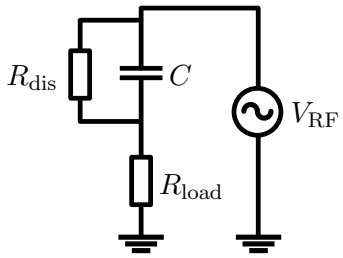

Fig. B.2: Circuit of bias-T with discharge resistor R_{dis}.

that inverts the system response to a pulse sequence reveals, that the offset voltage decays on a timescale $\tau_2 = R_{\text{dis}}C$ (compare Fig. B.3 (a)). Optimal conditions for the pulse shaping would require (i) $\tau_{RC} \sim T_p$, where $T_p \sim 50\,\text{ns}$ it the pulse width and (ii) $\tau_2 \ll T_{rep}$, where $T_{rep} \sim 500\,\text{ns}$ is the repetition time of the gates. Condition (i) results in $C \sim 1\,\text{nF}$ for fixed $R_{\text{load}} = 50\,\Omega$. Hence condition (ii) requires $R_{\text{dis}} \ll T_{rep}/C \sim 500\,\Omega$. However, keeping in mind that we want to eliminate the $1/f$ noise with the bias-T as high-pass filter, we see that the modified system transfer function flattens out below the frequency $f_2 = 1/(2\pi\tau_2)$ (see Fig. B.3 (b)) and does not efficiently block low frequency noise.

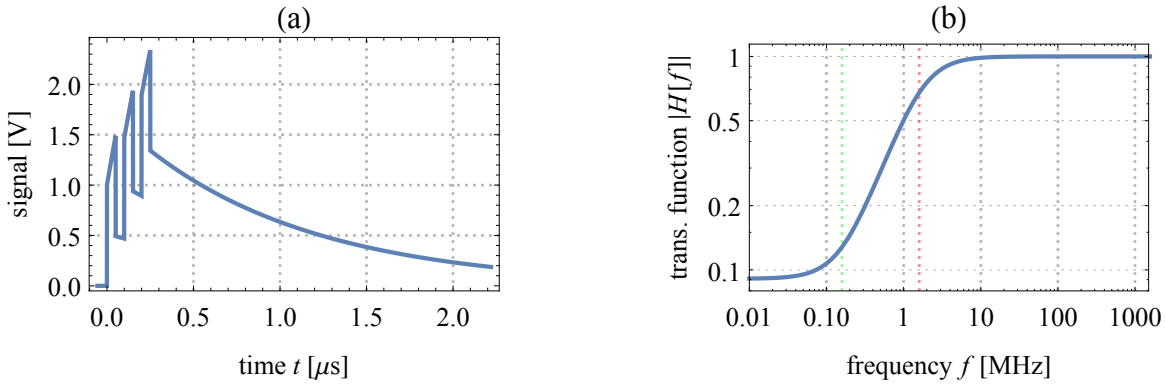

Fig. B.3: (a) Predistorted pulse train for optimal pulse shape at the load, according to circuit in Fig. B.2 with $R_{\text{dis}} = 500\,\Omega$ ($\tau_2 = 1\,\mu\text{s}$). (a) Frequency response of modified circuit. Dashed red line: cutoff frequency $f_c = 1.6\,\text{MHz}$; dashed green line: $f_2 = 0.16\,\text{MHz}$.

Appendix C

Filter Fitting Data

C.1 IIR Fitting Data

C.1.1 Demo Results

Fit #	A[mV]	B[mV]	τ[ns]
1	375.885	−3.832 34	3557.55
2	375.880	−2.432 06	484.388
3	375.878	−2.951 19	103.034
4	375.878	3.047 91	38.756
5	375.878	−0.309 75	38.5517
6	375.877	12.0045	9.675 11
7	375.878	−3.2689	8.914 96
8	375.877	17.6204	4.141 95
9	375.877	−7.576 13	4.3454
10	375.877	5.814 87	3.832 94
11	375.876	−2.218 21	4.467 24
12	375.877	0.472 652	6.920 11
13	375.877	−0.139 566	6.916 07

Table C.1: Full table of the IIR filter fitting parameter of all 13 fits of the demo dataset.

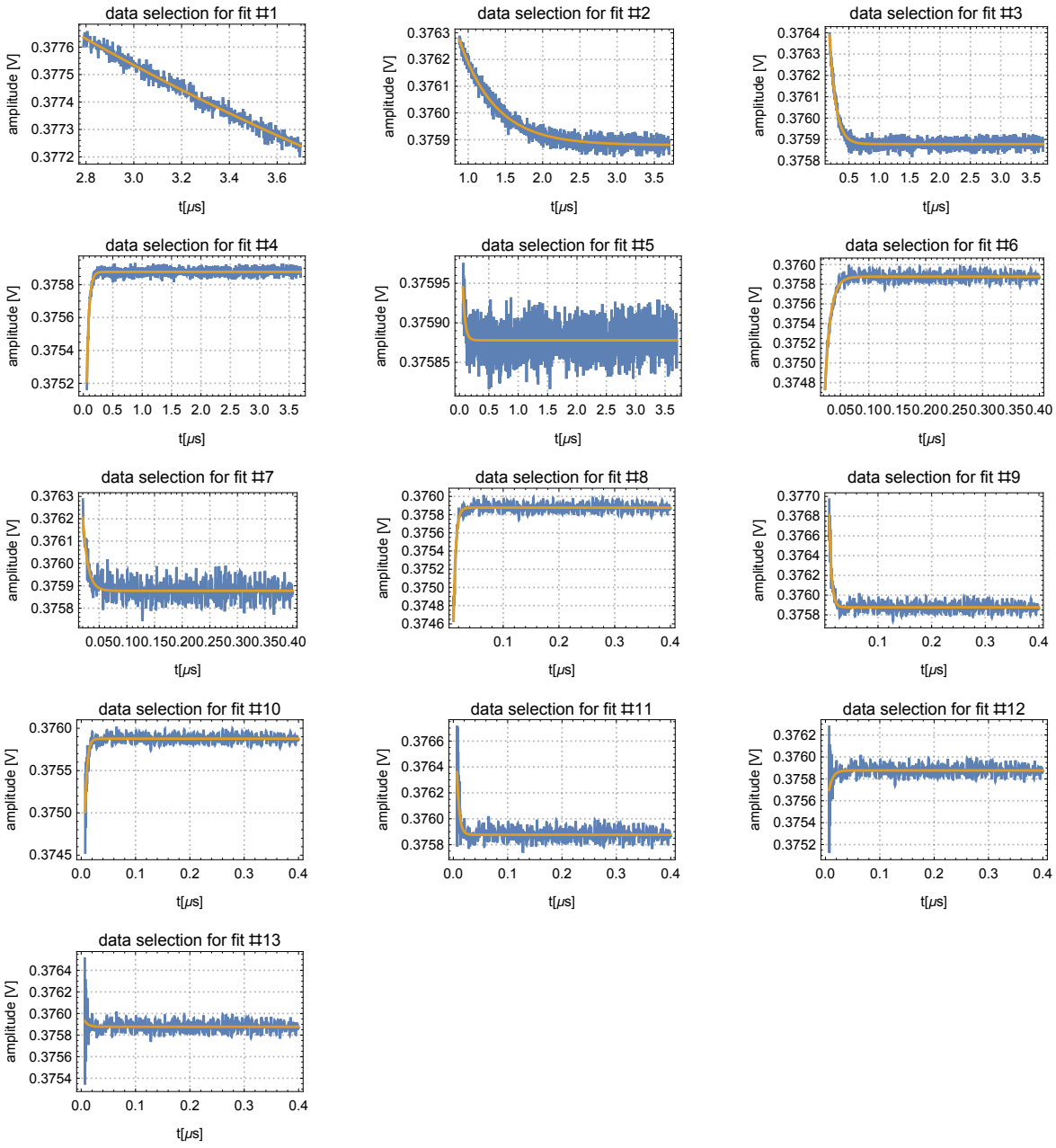

Fig. C.1: Plots of all IIR fits of the demo dataset.

Fit #	a_1	b_0	b_1
1	0.999 845	0.994 542	−0.994 387
2	0.998 861	0.993 596	−0.992 457
3	0.994 664	0.992 231	−0.986 895
4	0.985 652	1.008 12	−0.993 768
5	0.985 704	0.999 182	−0.984 887
6	0.942 393	1.032 04	−0.974 434
7	0.940 071	0.991 637	−0.931 708
8	0.868 525	1.045 95	−0.914 476
9	0.882 067	0.981 407	−0.863 474
10	0.862 874	1.014 64	−0.877 51
11	0.883 565	0.994 475	−0.878 04
12	0.922 723	1.001 21	−0.923 934
13	0.922 801	0.999 643	−0.922 444

Table C.2: Table of the IIR first-order filter coefficients extracted from the fits of the demo dataset.

C.1.2 Flux line 6

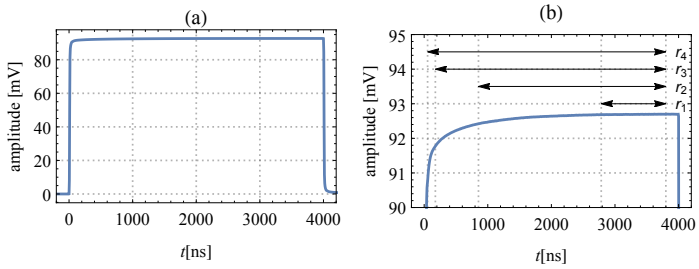

Fig. C.2: Fitting ranges of first four IIR fits for flux line 6.

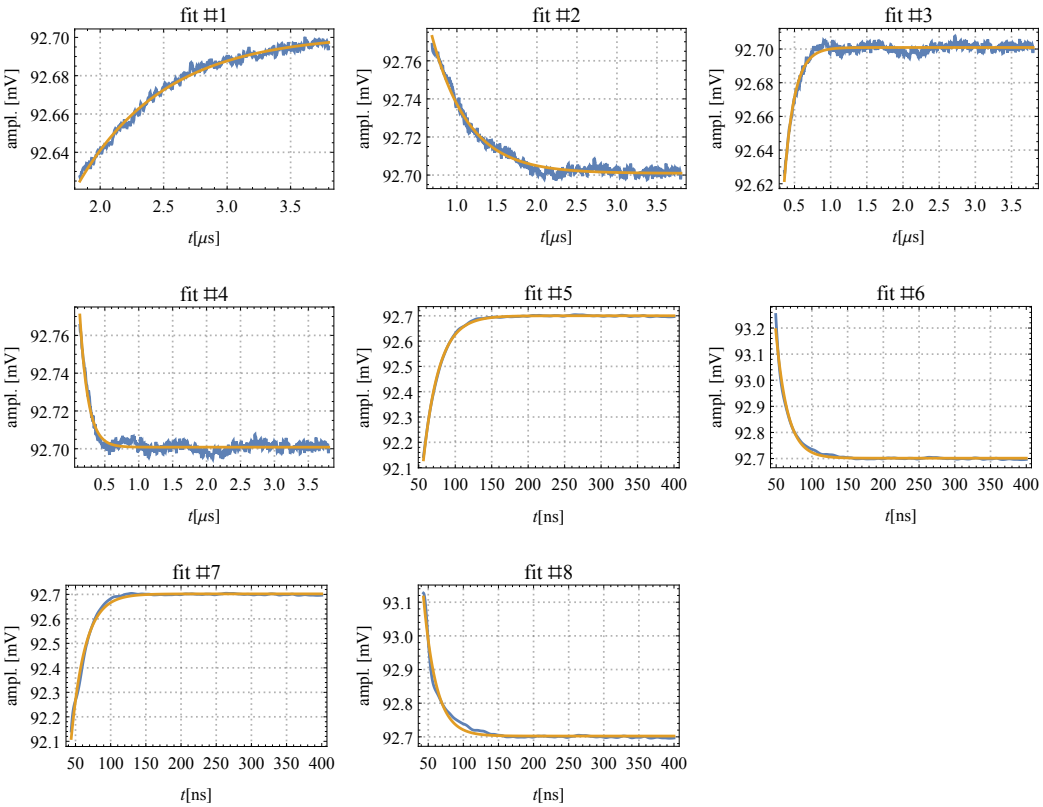

Fig. C.3: Plots of all IIR fits for flux line 6.

Fit #	A[mV]	B[mV]	τ[ns]
1	92.7017	1.140 06	681.852
2	92.7009	−0.328 385	454.185
3	92.7009	0.981 595	142.865
4	92.7008	−0.207 01	121.565
5	92.7002	7.965 49	21.3799
6	92.7014	−10.1549	16.3237
7	92.7021	5.304 27	19.995
8	92.7024	−4.402 38	18.2589

Table C.3: Table of the fitting parameters for flux line 6.

Fit #	a_1	b_0	b_1
1	0.998 763	1.012 42	−1.011 18
2	0.998 173	0.996 474	−0.994 647
3	0.994 122	1.010 67	−1.004 79
4	0.993 184	0.997 779	−0.990 963
5	0.958 249	1.092 04	−1.050 29
6	0.955 024	0.903 491	−0.858 515
7	0.956 749	1.059 38	−1.016 13
8	0.957 358	0.955 63	−0.912 989

Table C.4: Table of the IIR first-order filter coefficients extracted from the fits for flux line 6.

C.2 FIR fitting data

C.2.1 Demo Result

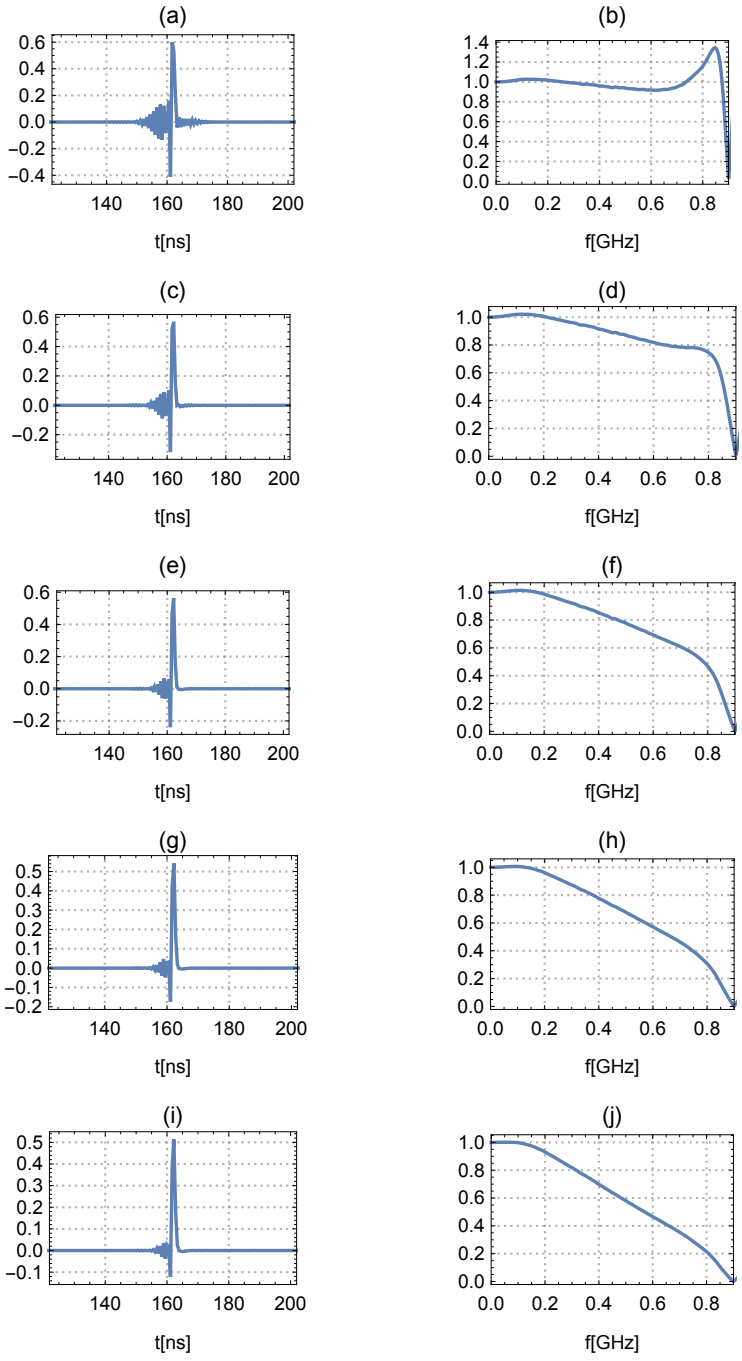

Fig. C.4: (a), (c), (e), (g), (i) are zooms to the peak of the FIR filters and (b), (d), (f), (h) and (j) power spectra of the FIR filters for the regularization parameters $\alpha = 0.2, 0.4, 0.6, 0.8, 1.0$ from top to bottom (demo dataset). Increasing the regularization parameter α results in low-pass filtering the FIR filter kernel as expected.

C.2.2 Flux Line 6

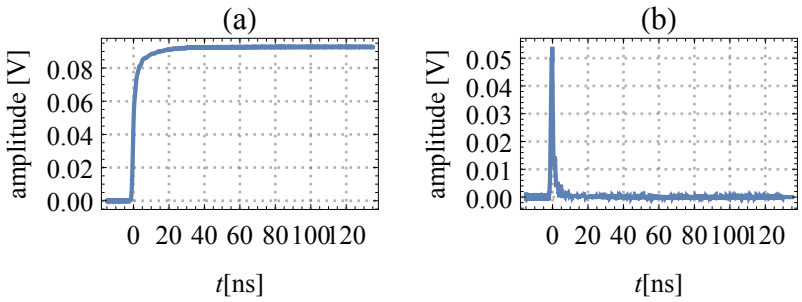

Fig. C.5: Flux line 6 data set: (a) IIR corrected data taken for FIR extraction. (b) Impulse response (of IIR corrected data) calculated by numerical differentiation of a step response (data in (a)).

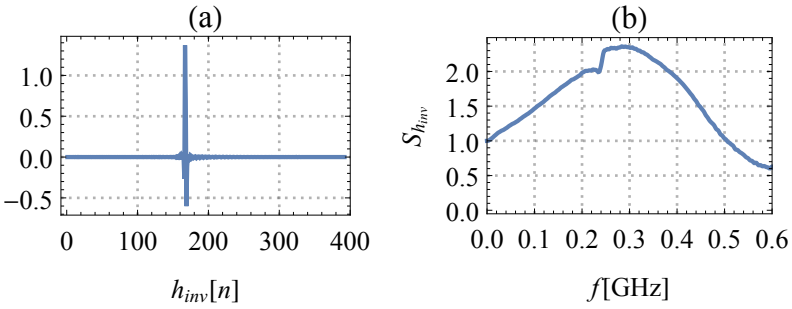

Fig. C.6: Flux line 6 data set: (a) FIR filter coefficients for regularization parameter $\alpha = 0.3$. (b) Power spectrum of the FIR filter coefficients.

ETH

Eidgenössische Technische Hochschule Zürich
Swiss Federal Institute of Technology Zurich

Declaration of originality

The signed declaration of originality is a component of every semester paper, Bachelor's thesis, Master's thesis and any other degree paper undertaken during the course of studies, including the respective electronic versions.

Lecturers may also require a declaration of originality for other written papers compiled for their courses.

I hereby confirm that I am the sole author of the written work here enclosed and that I have compiled it in my own words. Parts excepted are corrections of form and content by the supervisor.

Title of work (in block letters):

Shaping of Fast Flux Pulses for Two-Qubit Gates: Inverse Filtering

Authored by (in block letters):

For papers written by groups the names of all authors are required.

Name(s):	**First name(s):**
Butscher	Jonas

With my signature I confirm that

- I have committed none of the forms of plagiarism described in the 'Citation etiquette' information sheet.
- I have documented all methods, data and processes truthfully.
- I have not manipulated any data.
- I have mentioned all persons who were significant facilitators of the work.

I am aware that the work may be screened electronically for plagiarism.

Place, date	**Signature(s)**
03/01/2018	J. Butscher

For papers written by groups the names of all authors are required. Their signatures collectively guarantee the entire content of the written paper.